Electrochimica Acta 389 (2021) 138773

Contents lists available at ScienceDirect

Electrochimica Acta

journal homepage: www.elsevier.com/locate/electacta

Structural and electrochemical properties of undoped and In^{3+}-doped multi-phase zinc- antimony oxide for a high-performance pseudocapacitor

Duanghatai Raknual[a], Supparat Charoenphon[b,c], Pakpoom Reunchan[b,c], Auttasit Tubtimtae[d,*]

[a] Department of Chemistry, Faculty of Liberal Arts and Science, Kasetsart University, Kamphaeng Saen Campus, Nakhon Pathom, 73140, Thailand
[b] Department of Physics, Faculty of Science, Kasetsart University, Bangkok, 10900, Thailand
[c] Thailand Center of Excellence in Physics (ThEP Center), Ministry of Higher Education, Science, Research and Innovation, 328 Si Ayutthaya Road, Bangkok, 10400, Thailand
[d] Department of Physics, Faculty of Liberal Arts and Science, Kasetsart University, Kamphaeng Saen Campus, Nakhon Pathom, 73140, Thailand

ARTICLE INFO

Article history:
Received 16 February 2021
Revised 31 May 2021
Accepted 10 June 2021
Available online 13 June 2021

Keywords:
Indium doping
Multi-phase zinc-antimony oxide
Pseudocapacitor
Structural properties
Electrochemical properties

ABSTRACT

Pseudocapacitive charge storage devices based on undoped and In^{3+}-doped multi-phase zinc- antimony oxide (ZAO) with high potential insertion/removal processes of disulfide ions the electrodes were performed. The thin film morphologies related to a more regular grain shape, leading to enhanced surface mobility and nucleation density. The sizes of the nanoparticles (NPs) for undoped and In^{3+}-doped ZAO were uniformly distributed between ~ 100 – 500 nm. Based on electronic structure calculations, the In^{3+}-doped $ZnSb_2O_4$ behaves as a weak *p*-type semiconductor with a lower-than-band gap optical absorption and has greater charge storage performance diffused into the surface of electrode. This results in it obtaining a lower barrier layer and charge transfer resistance at the interface. In^{3+} doping in the ZAO electrode was driven in increments of energy density (77.34 Wh kg^{-1}), power density (13.92 kW kg^{-1}), specific capacitance (470 mAh g^{-1}@10 mV s^{-1}), and average capacitance retention (~87%). It is noted that the synthesized material in the present study and the importance of In^{3+} doping should be further considered for high-performance pseudocapacitor applications.

1. Introduction

Transition metal oxides (TMOs)-based thin film or nanoparticle semiconductors of various structural phases (i.e., molybdenum oxide (MoO_3) [1], bismuth oxide (Bi_2O_3) [2], tungsten oxide (WO_{3-x}) [3,4], vanadium pentoxide (V_2O_5) [5], copper oxide (CuO) [6], and manganese oxide (MnO_2) [7]) have attracted significant attention for electrodes in electrochemical energy storage applications, for instance as supercapacitors or pseudocapacitors due to their abundant, non-toxic, low-cost, and safe characteristics along with improving the specific capacitance and enhancing the capability of ionic charging and discharging behavior into the layer of electrodes by surface reversible redox pseudocapacitance reactions that occur at or near the surface of a material in contact with an electrolyte [8].

Supercapacitors (SCs) can typically be categorized into electric double-layer capacitors

(EDLC) and pseudocapacitor due to their different charge storage mechanism [9]. Among of them, pseudocapacitors have attracted greater attention due to their fast-reversible charge/discharge behavior, which can provide higher energy densities compared to EDLC [10,11]. Nonetheless, although SC-type materials have high specific capacity, they still show poor kinetics rate performance, poor conductivity, low stability, and low rate capability of the electrodes, which is related to the slow charge transfer and insertion and correspond to the sluggish phase change in the charge/discharge processes [12,13]. These have worsened the capacitive and electrochemical performance. To overcome these issues, numerous researchers have attempted to find the strategies to improve specific surface area by tuning in the nanoscale of morphological characteristics [14,15] and increase the volumetric capacitance based on higher mass loading with three-dimensional (3D) porous network [16]. These can serve to achieve excellent

* Corresponding author.
E-mail address: tubtimtae@gmail.com (A. Tubtimtae).

https://doi.org/10.1016/j.electacta.2021.138773
0013-4686/

capacitive rate performance along with high power density and energy density.

From our knowledge, ZnO is a widely used material with various industrial and technological applications, such as in optical and electronic devices [17]. Another application of ZnO is in electrochemical or energy storage devices. Consecutively, most *n*-type and *p*-type elements are usually also introduced in ZnO thin films to form ternary TMOs for a battery-type supercapacitor electrode, for example cobalt [18], aluminum [19], iron [20], boron [21], gallium [22], and chromium [23]. This leads to them having advantages in the form of an excellent structure and electrochemical properties for energy storage and capacitive devices.

Another spinel-ternary transition metal oxide material was explored for use in non-linear device applications [24], including electrochemical and energy storage devices, i.e. zinc antimony oxide (ZAO). ZAO is a typical ceramic material with excellent electrical/magnetic properties, high electrochemical/thermal stability, reversibility, and high specific capacitance [25,26]. In addition, ZAO also has a tetragonal crystal structure with the P42/mbc(135) space group and with cell parameters $a = b = 0.8527$ nm, $c = 0.5942$ nm [27]. Furthermore, ZAO is mineralogically known as ordenezite and crystallizes in trirutile-type structure, with the space group P41/mnm [28]. Most previous studies focus on the preparation of ZAO nanostructures including nanowires, nanobelts, and thin films [25], such as Aoki et al. which reported on *p*-type ZnO thin films obtained by Sb doping using the excimer laser diffusion method [29] and Zeng et al. which fabricated pinel-type $ZnSb_2O_4$ nanowires and nanobelts synthesized by an indirect thermal evaporation [30]. Consequently, performance improvement of ZAO in various applications has also been further treated by doping elements. From previous studies, Arunkumar et al. synthesized trirutile antimonate N - doped nanocrystalline $ZnSb_2O_6$ by a facile solution combustion method for photocatalytic activity enhancement [28]. Nanocrystalline Tb^{3+}/Eu^{3+}-doped $ZnSb_2O_6$ was synthesized by a facile sonochemical method for application as a white light emitter and as an efficient material for photocatalysis [31]. However, this material have currently been studied to as a promising electrochemical and energy storage material for supercapacitors based on its significant specific energy density, availability, and low cost [26]. The main purpose is to enhance the capacitive performance of the oxide electrodes by morphology modification, internal porous, and composite structure formations. For example, Balasubramaniam et al. synthesized Sn-doped $ZnSb_2O_6$ nanostructures as an electrode material using a chemical precipitation method for supercapacitors in order to investigate its electrochemical stability and potentiality as an energy storage material. The results indicate a significant specific capacitance of 222 F g^{-1} at a current density of 0.5 A g^{-1}. After charging and discharging over 1,000 cycles, the capacitance retention was enhanced to 105% which presents its stability and electrochemical activeness [32]. Additionally, graphene-doped $ZnSb_2O_6$ nanocomposites were prepared by the probe ultrasonication and precipitation methods. The maximum specific capacitance obtained was 1470.25 F g^{-1} at a current density of 1 A g^{-1} with capacitance retention of 100%, while during the cyclic period the capacitance increased to 105% and 110% [33].

In the present study, zinc antimony oxide (ZAO, $ZnSb_2O_4$) was synthesized via Sb^{3+} doping in ZnO using the dropped casting and screening method from the wet chemical solution due to it provides simple preparation, inexpensiveness, and eco-friendliness. Indium (In^{3+}) was also doped into the ZAO material to compare performance. The specific capacitance of the ZAO electrode of 434 mAh g^{-1} was obtained and increased to 470 mAh g^{-1} after In^{3+} doping in the ZAO electrode at a scan rate of 10 mV s^{-1}, which is increasing 8.3%. The increment of ~ 1.4 fold in energy density and power density was also obtained after In^{3+} doping with a capacitance retention and coulombic efficiency of ~ 81 and 93% after 150 cycles, respectively. In addition, the electronic structure calculations based on density-functional theory (DFT) were performed to understand the fundamental properties and possibility of In doping in ZAO. The overall results clearly indicate that this newly demonstrated electrode material with In^{3+} doping has a potential use as a pseudocapacitor and in future energy storage devices.

2. Experimental section

2.1. Preparation of undoped and In^{3+}-doped multi-phase zinc-antimony oxide thin films

The starting materials for the synthesis of multi-phase zinc-antimony oxide thin films were 0.12 g sodium hydroxide (NaOH, 98%, Fisher Chemical) mixed with 0.228 g antimony (III) chloride ($SbCl_3$, ≥ 99.95%, Aldrich) in 10 mL deionized water (DI water) and then vigorously stirred for 10 min until a white precipitate of the solution was formed. The reaction of the synthesis for Sb^{3+} ions is depicted as:

$$SbCl_3 + 3NaOH \rightarrow Sb(OH)_3 + 3NaCl \quad (1)$$

$$Sb(OH)_3 \rightarrow Sb^{3+} + 3OH^- \quad (2)$$

The precipitate of antimony (III) hydroxide ($Sb(OH)_3$) was filtered by filter paper and transferred onto a slide glass, followed by heating at 80 °C until it dried. The precipitate was then scratched out from the slide glass to form a powder, which is the precursor of Sb^{3+} ions.

The $Sb(OH)_3$ powder was mixed with 5 g of zinc oxide powder (ZnO, 99%, Loba Chemie) in 25 mL DI water and vigorously stirred again for 2 h until a homogeneous white Zn-Sb-O solution was formed, which is the precursor of Zn^{2+}, Sb^{3+}, and O^{2-} ions. This homogeneous solution was filtered to obtain a white precipitate and transferred again onto a slide glass which was kept heated to 80 °C until it dried. After scratching out the precipitate from a slide glass to form a powder, the Zn-Sb-O powder was then transferred into an alumina cup which was sintered continuously in a high temperature furnace at 550 °C for 1 hour, as in the following reaction:

$$2Sb + (3/2)O_2 + ZnO \rightarrow ZnSb_2O_4 \quad (3)$$

To form undoped and In^{3+}-doped Zn-Sb-O thin films, 0.3 g of Zn-Sb-O powder was mixed with 0.2 g polyethylene glycol (PEG 300,MERCK premium quality Synthesis Grade) in 2 mL of ethanol and 2 mL of α-terpineol (90%, Aldrich). Finally, a mixed precursor was vigorously stirred for 20 min and then the Zn-Sb-O solution was dropped cast and screened onto a cleaned fluorine-doped tin oxide (FTO) glass substrate with a dimension of 10 × 10 mm^2. Later, an undoped Zn-Sb-O coated FTO glass substrate was heated at 100 °C for 6 hour to form a ZAO thin film on the FTO glass substrate. To compare performance, various concentrations (wt%) of indium (III) chloride ($InCl_3$, 99.995%, Acros Organics) were added into the above-mixed precursor to form the In^{3+}-doped Zn-Sb-O solution, followed by a similar procedure to form an In^{3+}-doped ZAO thin film on the FTO glass substrate. The Tafel plot was illustrated from the rising part of the cyclic voltammetry curve of each indium doping concentration and shown in Fig. S1 in the supplementary information. The intercept on the *y*-axis of linear fit was observed to investigate the highest exchange current density (J_0) for the optimal concentration of indium doping in the ZAO electrode. The J_0 values are depicted in Table S1.

2.2. Characterization

The undoped and In^{3+}-doped ZAO thin films were characterized using field-emission scanning electron microscopy (FESEM, JEOL, JSM-6301 F) and high-resolution transmission electron microscopy (HRTEM, FEI–Tecnai G^2 20 S-TWIN) operating at 200 kV. Energy dispersive spectroscopy (INCA, PentaPET × 3) was used to examine the stoichiometry of elements of the thin films. X-ray photoelectron spectroscopy (XPS) analysis was also used to detect the chemical states in the as-prepared thin films using an AXIS Ultra DLD (Kratos Analytical Ltd.) with a soft X-ray beam produced from a source of monochromated Al Kα anode. The energy of incident photons was 1486.6 eV, which was calibrated based on the work function and the Fermi energy level (E_f) of the spectrometer. The resultant XPS spectra were calibrated against the C1s photoelectron peak with binding energy of 285 eV from contamination, in order to compensate for any charge-induced shifts. The crystal structure was characterized by X-ray diffractometer (XRD) of $\lambda = 1.5406$ Å with Cu-Kα radiation (D8 Advance, Bruker AXS) in the range $20° \leq 2\theta \leq 80°$ with a resolution of 0.01°.

Furthermore, a Brunauer-Emmett-Teller (BET) surface area analyzer (Micrometrics, TriStar II 3020) was used to determine their adsorption capacities and physiochemical properties. The undoped and In^{3+}-doped ZAO powders were pretreated before measurement with ultrahigh purity N_2 as absorptive gas at a bath temperature of 77.3 K (-195.85°C). Finally, the vibrational mode of elements in the thin films was performed using Fourier Transform Infrared spectroscopy (FTIR, PerkinElmer Frontier™).

2.3. Electrochemical measurements

Electrochemical measurements were performed using a three-electrode configuration with an electrochemical analyzer (PGSTAT101, Metrohm Autolab). Various scan rates of 10, 30, 50, 70, and 100 mV s^{-1} was used for the experiment. An undoped or In^{3+}-doped ZAO thin film as a working electrode, a CuS counter electrode (CE), and an Ag/AgCl reference electrode were immersed in a polysulfide electrolyte solution consisting of 0.25 M $Na_2S{\bullet}9H_2O$, 1 M Sulfur, 0.2 M KCl, and 0.1 M KI dissolved in a methanol/water (7:3 v/v) solution to obtain oxidation and reduction peaks from a cyclic-voltammetry measurement. A CuS CE was prepared by a drop-cast method of a 0.5M $Cu(NO_3)_2{\bullet}3H_2O$ methanol solution and followed by a 1 M $Na_2S{\bullet}9H_2O$ methanol and DI water (7:3 v/v) solution onto a cleaned FTO glass for four cycles. Then the CuS-layered FTO glass was heated at 120°C for 30 min on a hotplate in ambient air, followed by cooling to room temperature [34]. Electrochemical impedance spectroscopy (EIS) measurement was performed via a Metrohm Autolab instrument (model PGSTAT302 N) in the range of 100 kHz – 100 mHz, at an applied potential of −0.1 V with an oscillation amplitude of 5 mV. The mass of the undoped and In^{3+}-doped ZAO thin films was measured using a four decimal place balance (OHAUS Corporation, USA).

2.4. Computational methods

To investigate the electronic structure of pristine and In^{3+}-doped ZAO, we employed density-functional calculations within the generalized gradient approximation (GGA) proposed by Perdew Burke and Ernzerhof (PBE) [35] as implemented in the Vienna *ab-initio*-simulation package (VASP) code [36]. Projector-augmented wave potentials with 12, 5, and 6 valence electrons for Zn ($3d^{10}4s^2$), Sb($5s^25p^3$), and O ($2s^22p^4$) were adopted to describe ionic-core-valence electron interactions. The calculated band gap based on PBE functional is 2.74 eV, smaller than the experimental value of 4.70 eV [24]. The local and semi-local functionals such as GGA are well known to significantly underestimate the band gap of metal oxides, partially due to the self-interaction error in DFT. The test calculations based on screened hybrid-functional—which partially correct the band gap and improve the defect levels compared to GGA functional—indicate that the core results for the electronic structure remain. Here, we focused on ZAO in tetragonal crystal structure with chemical formula Zn_2SbO_4 (space group $P4_2/mbc$). A primitive cell of Zn_2SbO_4 which consist of 8 Zn atoms, 4 Sb atoms, and 16 O atoms was used in the calculations of pristine Zn_2SbO_4. A 3 × 3 × 3 mesh of special Monkhost-Pack *k*-point was employed for the Brillouin zone integration. The energy cutoff for the plane-wave expansion was set to 520 eV. To simulate In^{3+}-doped $ZnSb_2O_4$, a 56-atom supercell which is 1 × 1 × 2 repetition of the 28-atom primitive cell was adopted and a 2 × 2 × 2 mesh of special Monkhost-Pack *k*-point was employed for the Brillouin zone integration. All atoms were relaxed until the residual forces were smaller than 0.02 eV/ Å.

The likelihood of the In impurities formation can be determined by the formation energy of a defect as a function of the Sb and In atomic chemical potentials ($\tilde{\mu}_{Sb}, \tilde{\mu}_{Zn}$) for all possible charge state. For instance, the formation energy of In_{Sb} in charge state q is defined by:

$$E_f\left(\mathrm{In}_{\mathrm{Sb}}^{q}\right) = E_{tot}\left(\mathrm{In}_{\mathrm{Sb}}^{q}\right) - E_{tot}\left(\mathrm{ZnSb_2O_4}\right) - [\tilde{\mu}_{In} + E_{tot}(In_{metal})] + [\tilde{\mu}_{Sb} + E_{tot}(Sb_{metal})] + q(E_F + E_V) \quad (4)$$

where $E_{tot}(\mathrm{In}_{\mathrm{Sb}}^{q})$ is the total energy of the supercell with an In atom substituted for Sb (In_{Sb}) and $E_{tot}(ZnSb_2O_4)$ is the total energy of the defect-free supercell. The indium atom is taken from reservoir with energy $\mu_{In} = \tilde{\mu}_{In} + E_{tot}[In_{metal}]$ and the Sb atom is placed in a reservoir with energy $\mu_{Sb} = \tilde{\mu}_{Sb} + E_{tot}[Sb_{metal}]$. The chemical potential ($\tilde{\mu}$) can vary to represent the experimental conditions during growth or annealing, which can range from O-rich (Sb-poor) to O-poor (Sb-rich) condition. In equilibrium growth of $ZnSb_2O_4$, the chemical potentials $\tilde{\mu}_{Zn}$, $\tilde{\mu}_{Sb}$ and $\tilde{\mu}_O$ must satisfy the stability condition $\tilde{\mu}_{Zn} + 2\tilde{\mu}_{Sb} + 4\tilde{\mu}_O = \Delta H_f(ZnSb_2O_4)$, where $\Delta H_f(ZnSb_2O_4)$ is the enthalpy of the formation of $ZnSb_2O_4$. Our calculated $\Delta H_f(ZnSb_2O_4)$ was ~ −9.56 eV. Their values were taken with respect to the total energy per atom of Zn, Sb and O_2 molecules. The chemical potential $\tilde{\mu}_{Zn}$, $\tilde{\mu}_{Sb}$ and $\tilde{\mu}_O$ are also subject to bounds in order to avoid the formation of secondary phases which are ZnO, ZnO_2, Sb_2O_3, Sb_2O_5 and SbO_2. The O-rich and O-poor conditions corresponded to the oxygen chemical potential of $\tilde{\mu}_O = 0$ and $\tilde{\mu}_O = [\Delta H_f(ZnSb_2O_4) - \tilde{\mu}_{Zn} - 2\tilde{\mu}_{Sb}]/4 = -1.10$ eV as shown as point A and C, respectively in Fig. S2. The indium chemical potential is limited by the formation of In_2O_3, $\tilde{\mu}_{In} = (\Delta H_f(In_2O_3 - 3\tilde{\mu}_O))/2$. For the experimental growth condition, the oxygen chemical potential $\tilde{\mu}_O$ was estimated to be −0.78 eV as shown in Fig. S2. The detail for the estimation is illustrated in the supplementary information. The formation energy also depends on the energy of the electron reservoir in $ZnSb_2O_4$ or Fermi level E_F, which is referenced to the valence band maximum (VBM) of the host material (E_V).

3. Results and discussion

3.1. Morphological characteristics and chemical compositions

As-grown nanoparticles (NPs) of undoped and In^{3+}-doped ZAO are shown by FESEM micrograph in Figs. 1(a,c), respectively. The clearly visible similar characteristics did not change substantially and agglomerated crystalline NPs were formed, both before and after In^{3+} doping. The grain boundaries were also clearly observed, which is related to a more regular grain shape, leading to an enhancement of surface mobility and nucleation density. The size of NPs for undoped and In^{3+}-doped ZAO were ~ 100 −500 nm and uniformly distributed on the surface of the FTO glass substrate. Yet

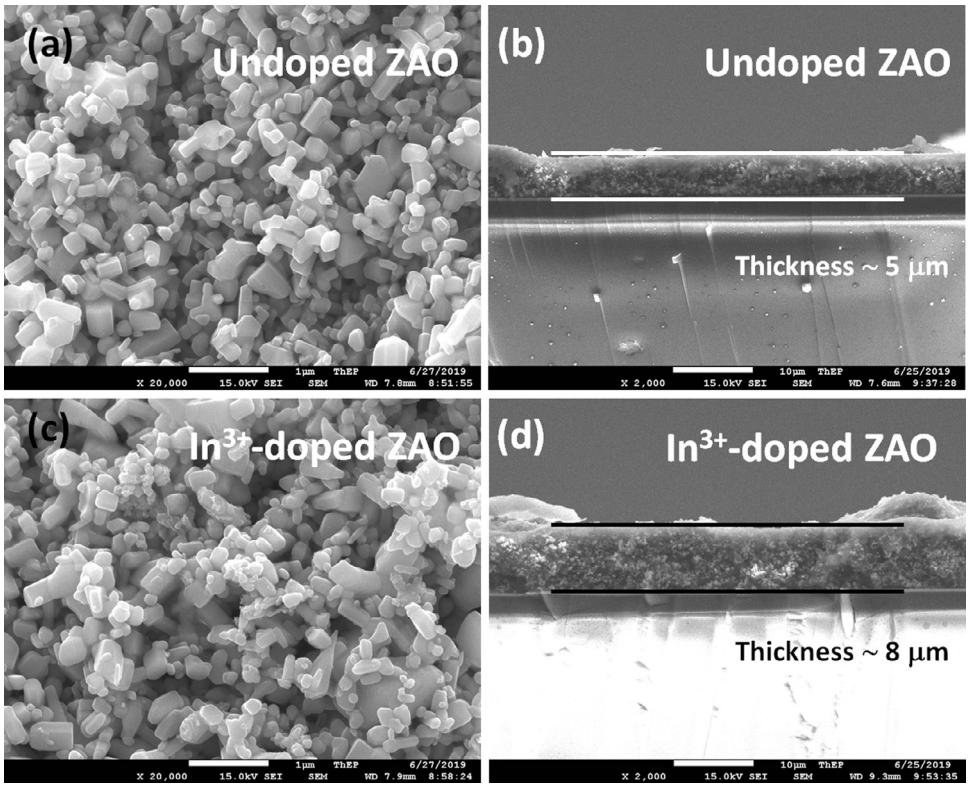

Fig. 1. FESEM micrographs of (a,c) surface morphologies and (b,d) cross sectional images ofthe undoped and In^{3+}-doped ZAO thin films, respectively.

aggregated, rougher interparticles and the high porosity of both undoped and In^{3+}-doped ZAO NPs facilitate electrolyte penetration and can obtain faster ion transportation through the surface of the electrodes, leading to better electrical conductivity and may help it to have good capacitive behavior [37]. The thicknesses of the undoped and In^{3+}-doped ZAO thin films in Figs. 1(b,d) were determined from the cross-sectional images, which were ~ 5 and 8 µm, respectively.

The characteristics of the undoped and In^{3+}-doped ZAO NPs were also investigated and confirmed using HRTEM images in Figs. 2(a–b), respectively. This reveals that the size and characteristics of the undoped and In^{3+}-doped ZAO NPs are similar to the images in the FESEM micrograph in Figs. 1(a,c). Next, Figs. 2(c–d) illustrate the selected region of the undoped and In^{3+}-doped ZAO NPs, and inter planar *d*-spacing was observed of 2.38 and 2.40 Å, respectively, corresponding to the (311) plane. Fig. 3 shows the chemical composition of the undoped and In^{3+}-doped ZAO electrodes. The EDS spectrum in Fig. 3(a) shows the weight and atomic percentages of each chemical composition and confirms the presence of O, Zn, and Sb in the electrode. The presence of In in the spectrum (Fig. 3(b)) confirms the successful doping of In^{3+} into the ZAO electrode.

3.2. Structural characteristics

The as-prepared undoped and In^{3+}-doped ZAO thin films were examined by XRD patterns, as shown in Fig. 4. For the undoped ZAO thin film, all the observed diffraction peaks were found of Sb^{3+}-doped ZnO and it can be indexed the possible multi-phases as tetragonal $ZnSb_2O_4$ with a space group of P42/mbc(135) (JCPDS no. 075-2184, $a = b = 8.5270$ Å, and $c = 5.9420$ Å), corresponding to the plane of (311), (204), and (423) at $2\theta = 36.56°$, 66.61°, and 68.20°, respectively. Further, tetragonal $ZnSb_2O_4$ with the same space group (JCPDS no. 088-2118, $a = b = 8.5010$ Å, and $c = 5.9210$ Å), corresponding to the plane of (420) and (523) at $2\theta = 47.83°$ and 77.19°, respectively. Moreover, the secondary phase of tetragonal $ZnSb_2O_6$ with a space group of P-4n2(118) (JCPDS no. 003-0455, $a = b = 6.5980$ Å, and $c = 5.1670$ Å) was found at $2\theta = 34.72°$ for the (002) plane, and finally the third phase of orthorhombic $Zn_7Sb_2O_{12}$ with a space group of Cmma(67) was observed at the 2θ position of 56.87° and 63.12°, which are in good agreement to the planes of (623) and (592), respectively (JCPDS no. 036-1445, $a = 12.1030$ Å, $b = 18.5590$ Å, and $c = 8.5180$ Å). All diffraction peaks were observed with lower intensity and shifted to the lower 2θ position after In^{3+} doping. This may be due to more observed aggregation and interconnect of NPs and consistent with the previous report of P. Suttiyarak et al. [38]. The main peak of the (311) plane of undoped and In^{3+}-doped ZAO was investigated for the lattice parameters ($a = b$, and c) and inter planar *d*-spacing value. The calculated lattice parameters ($a = b = 8.144$ Å, and $c = 4.911$ Å) and $d_{(311)} = 2.456$ Å were obtained for undoped ZAO compared with $a = b = 8.207$ Å, and $c = 4.949$ Å) and $d_{(311)} = 2.474$ Å for In^{3+}-doped ZAO. A slightly higher value of lattice parameters and inter planar *d*-spacing is agreed with the previous reported literatures of J.U. Brehm et al. [39], E.N.A.A. Armah et al. [40], and P. Suttiyarak et al. [41], which are likely associated with the larger ionic radius of In^{3+} (0.80 Å) than the ionic radii of Zn^{2+} (0.74Å) and Sb^{3+} (0.76Å) [42]. However, this occurrence leads to more randomly oriented crystallites, contributing to more micro-strain and lattice disorder in the ZAO structure, which may provide more surface grains, pore volume, and increase the total defect creation energy with respect to the bulk crystal because these grains generate additional interface surface area, as the In^{3+} ions acting as Frenkel defects in the ZAO lattice [43]. This may also attribute to more inducing the morphological transformation [44]. Yet the two binary phases of Sb_2O_3 and Sb_2O_4 that were observed in the XRD patterns may be due to imperfect growth during the material synthesis.

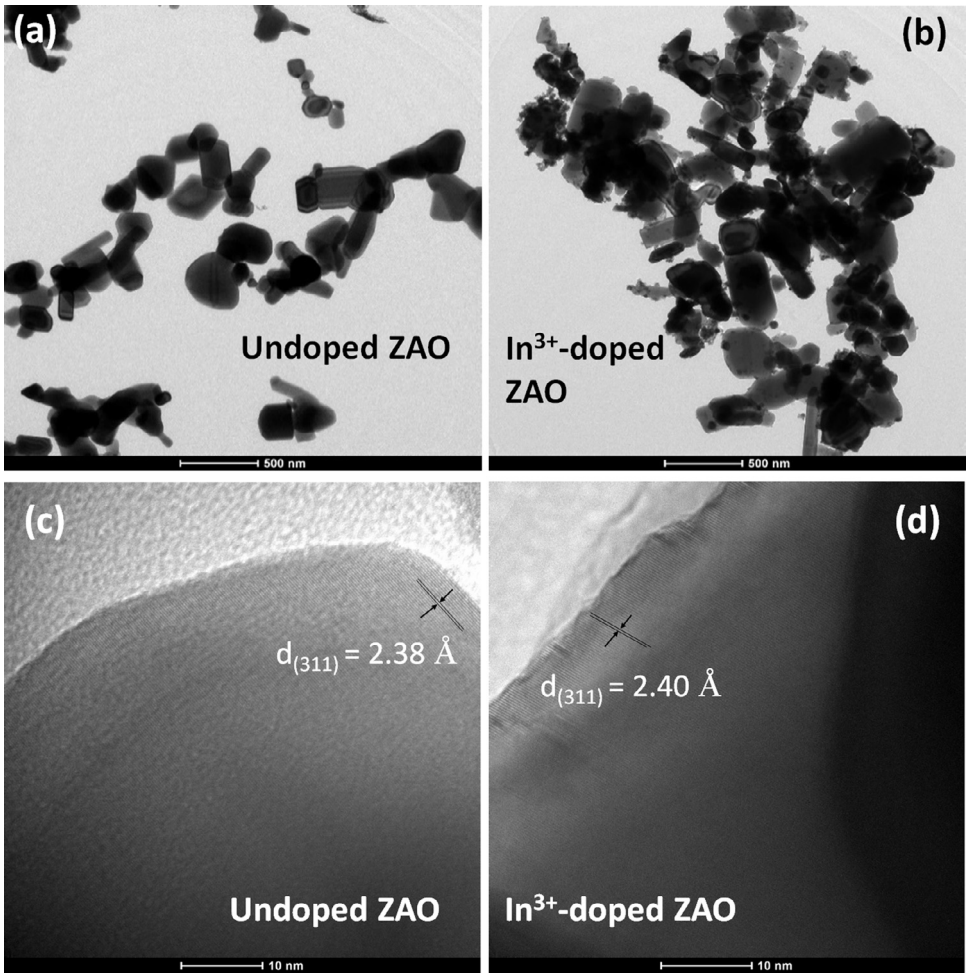

Fig. 2. TEM images in bright field imaging mode of (a,b) nanoparticle characteristics and (c,d) the HRTEM lattice images of undoped and In^{3+}-doped ZAO NPs, respectively.

3.3. XPS analysis

Chemical compositional analysis was investigated by XPS. Figs. 5(a-b) show the survey scan spectral in the wide range of undoped and In^{3+}-doped ZAO, respectively, and it is apparent that the undoped ZAO thin film is composed of Zn, Sb, and O (KLL) photoelectron lines. The O KLL region shows that the oxygen atoms were incorporated in the sample [45]. The C 1s spectrum gives a peak at 284.5 eV, attributed to bonds between sp^2 hybridized carbon atoms [46]. Meanwhile, the In^{3+}-doped ZAO thin film constitutes Zn, Sb, O (KLL), and In photoelectron lines without any observed impurities. The peaks for the Zn $2p_{3/2}$ and Zn 2 $p_{1/2}$ (Fig 5(c)) are respectively centered at 1020.8 eV and 1043.9 eV, corresponding to the binding energy of Zn^{2+} in the sample and the spin energy separation of Zn $2p_{3/2}$ and Zn $2p_{1/2}$ is found to be 23.1 eV. The results indicate that the chemical valence of Zn is +2 oxidation state [47]. A $Sb3d_{5/2}$ region (Fig. 5(d)) was observed at the binding energy of 531.3 eV and suggested that the oxidized antimony corresponds closely to bulk Sb_2O_3 [48]. The O 1s region in Fig. 5(e) shows the peak at 530.6 eV, which is attributed to Zn-O lattice oxygen (O_L) [49]. Finally, the oxidation states of In in ZAO lattice in Fig. 5(f) were deconvoluted to In $3d_{5/2}$ at 443.7 eV and In $3d_{3/2}$ at 449.9 eV, corresponding to indium oxide hydroxide (InOOH) and indium hydroxide ($In(OH)_3$), respectively, and these can be transformed to indium oxide (In_2O_3) [50].

3.4. BET surface analysis

The equilibrium N_2 adsorption-desorption isotherms curves of undoped and In^{3+}-doped ZAO are displayed in Figs. 6(a) and 6(d), respectively. The isotherm curves provide an increasing adsorption curve and then decline sharply in a desorption curve at the saturation pressure. The characteristics of these isotherm curves can be ascribed to the type II shape of the Brunauer–Deming–Deming–Teller (BDDT) classification. This classification indicates that the ZAO thin films consisting of interconnected mesoporous structures and N_2 adsorption occurred in these structures [51], corresponding with the pore-size distribution calculated using the Barrett–Joyner–Halenda (BJH) method in Figs. 6(b) and 6(e), respectively. Furthermore, the linear multipoint Brunauer-Emmet-Teller (BET) plots for nitrogen adsorption are shown in Figs. 6(c) and 6(f). The parameter values of the BET surface area analysis are also depicted in Table 1 for undoped and In^{3+}-doped ZAO electrodes, respectively. The pore structure alteration (pore volume, pore size, and micropore area) after In^{3+} doping can be further confirmed by the larger pore size distribution of the ZAO thin film. The lower surface area to volume ratio after In^{3+} doping in ZAO due to the slightly larger pore volume ratio (~ 1.20 times) than that of the ratio of a micro pore area (~ 1.14 times). This is explained in Section 3.2 by the influence of In^{3+} doping acting as Frenkel defects in the ZAO structure.

Table 1
Parameter values obtained from BET surface analysis.

Electrode	Surface area / $m^2\ g^{-1}$	Pore volume / $cm^3\ g^{-1}$	Pore size / nm	Micropore area / $m^2\ g^{-1}$	BJH adsorption average pore diameter / nm	BJH desorption average pore diameter / nm	Surface area to volume ratio / $m^2\ cc^{-1}$
Undoped ZAO	4.50	0.0096	8.54	2.29	11.76	11.81	238.54
In^{3+}-doped ZAO	5.06	0.0115	9.08	2.61	12.08	12.22	226.96

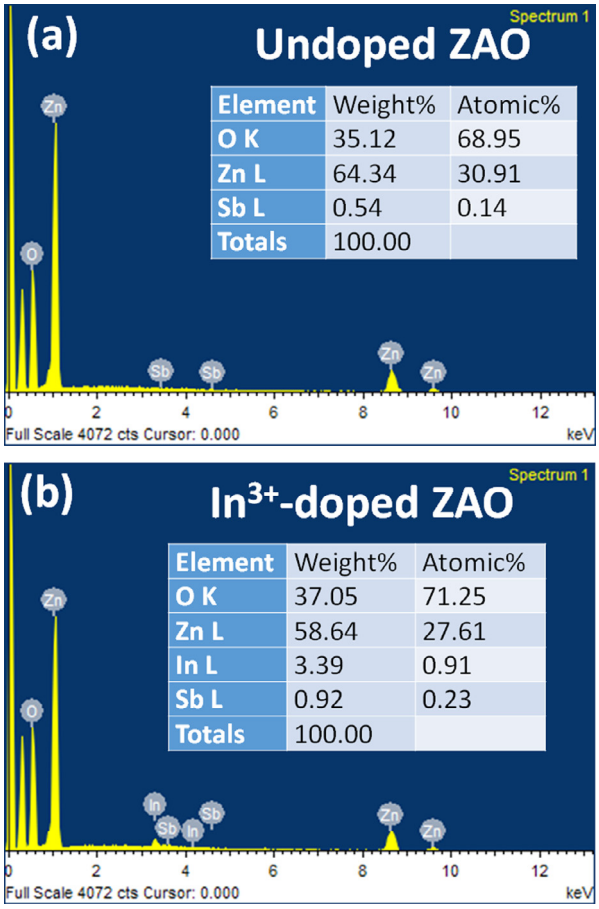

Fig. 3. EDS spectra of (a) undoped and (b) In^{3+}-doped ZAO thin films.

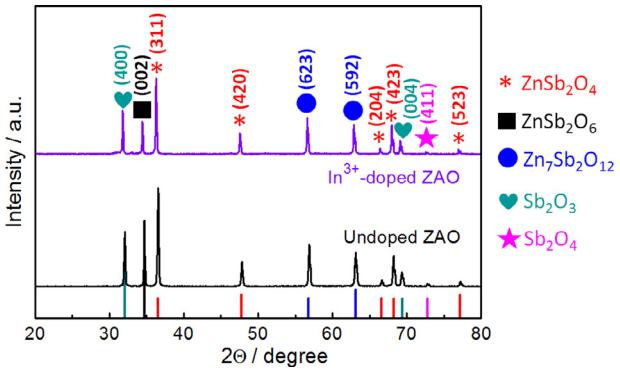

Fig. 4. XRD patterns of the undoped and In^{3+}-doped ZAO thin films.

3.5. FTIR analysis

The FTIR spectra of undoped and In^{3+}-doped ZAO are shown in Fig. 7 and indicate that the peaks at 470 cm^{-1} and ranging from 440 cm^{-1} to 540 $cm^{-1}$for undoped and In^{3+}-doped ZAO are assigned to the stretching mode wurtzite lattice vibrations of metal-oxygen bonds of Zn–O [24,26,52]. The peaks at 796 and 881 cm^{-1} correspond to Sb–O stretching vibration [53] and the deformation vibrations of the C–C bond [54], respectively. The two bands observed at 918 and 1050 cm^{-1} could be assigned to δ SbOH deformation modes [55]. The peaks at 1374 and 1739 cm^{-1} are assigned to wagging of CH^{2+} group and the existence of the COO– ion in Zwitter ionic form [56]. The bands characteristic to the C–H bond appear in the ranges ~ 1400–1500 cm^{-1} and 2800–3000

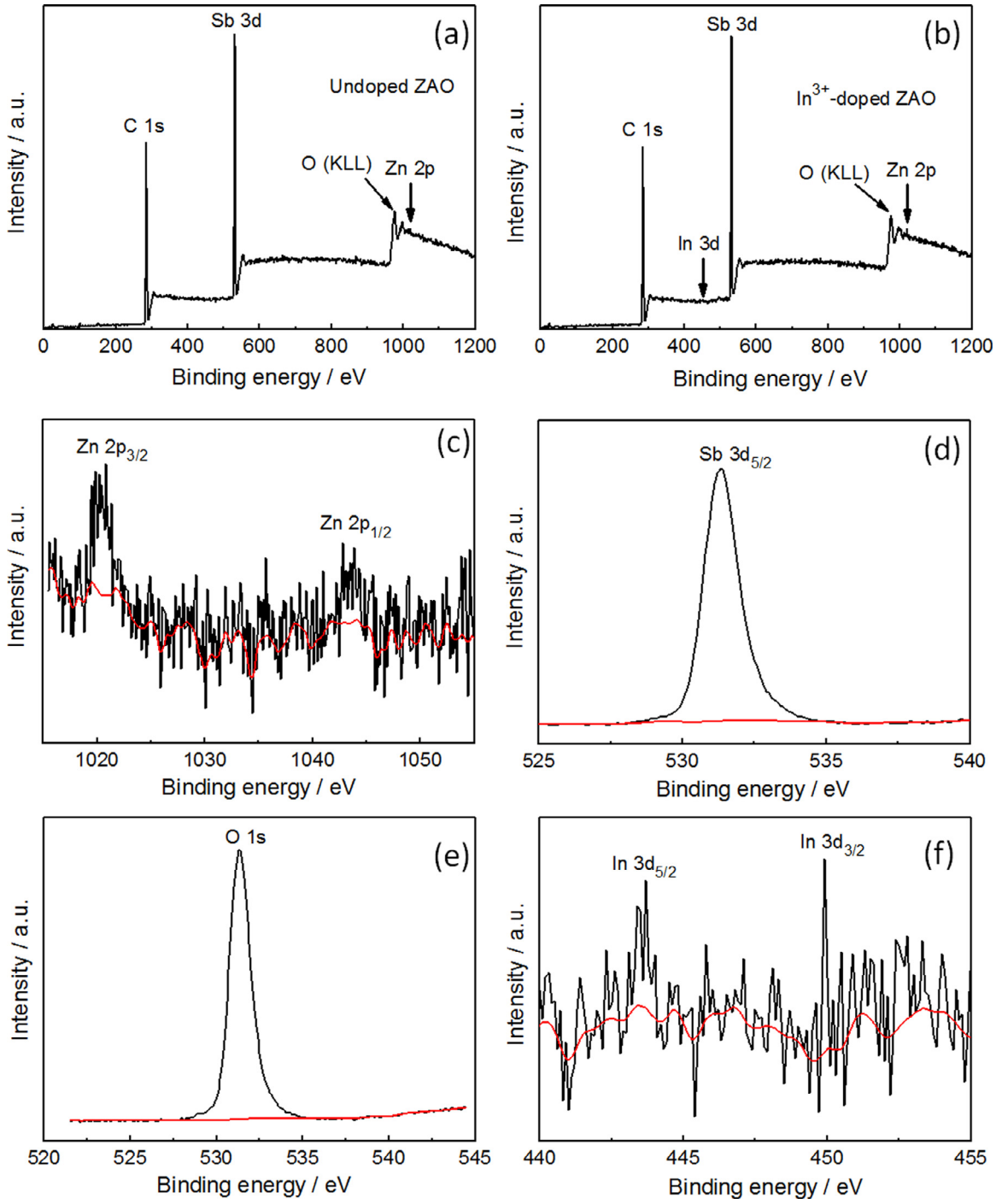

Fig. 5. XPS spectra survey scan of (a) undoped and (b) In^{3+}-doped ZAO. The deconvoluted spectra of (c) Zn 2p, (d) Sb 3d, (e) O 1s, and (f) In 3d.

cm^{-1}, which are attributed to the–CH2– groups [57]. Finally, the broad absorption band peak at 3462 cm^{-1} is due to the stretching vibration of O–H [58]. In the case of In^{3+} doping in the ZAO thin film, the intensity of most peaks are slightly reduced and may be due to the formation of In NPs on the surface of the ZAO thin film, similar to previous works in Ref. [52,59].

3.6. Density-functional calculations of In^{3+}-doped $ZnSb_2O_4$

Fig. 8 shows the 28-atom primitive cell of $ZnSb_2O_4$ which is isostructural to "red lead" (Pb_3O_4). Here, $ZnSb_2O_4$ is crystallized in the space group of $P4_2/mbc$ similar to Pb_3O_4. In this crystal structure, Zn atoms are at 8*h* Wyckoff position, connecting pyramidally with three nearest-neighbors oxygen and Sb atoms are at 4*d* Wyckoff position, forming a distorted tetrahedron with six nearest neighbor oxygen. Only a few materials, including $TiSn_2O_4$, $CoSb_2O_4$, and $SnPb_2O_4$ [60] are formed in this unique crystal structure. A noticeable hollow in the center of the crystal structure is suggested to be stabilized by the van der Waals interactions between the lone pair electron [61].

Based on GGA-PBE, the calculated lattice parameters *a* and *c* are 8.656 and 6.081 Å, respectively, slightly larger than the experimental values of $a = 8.5270$ Å (JCPDS no. 075-2184) or $a = 8.5010$ Å (JCPDS no. 088-2118) and $c = 5.9420$ Å (JCPDS no. 075-2184) or

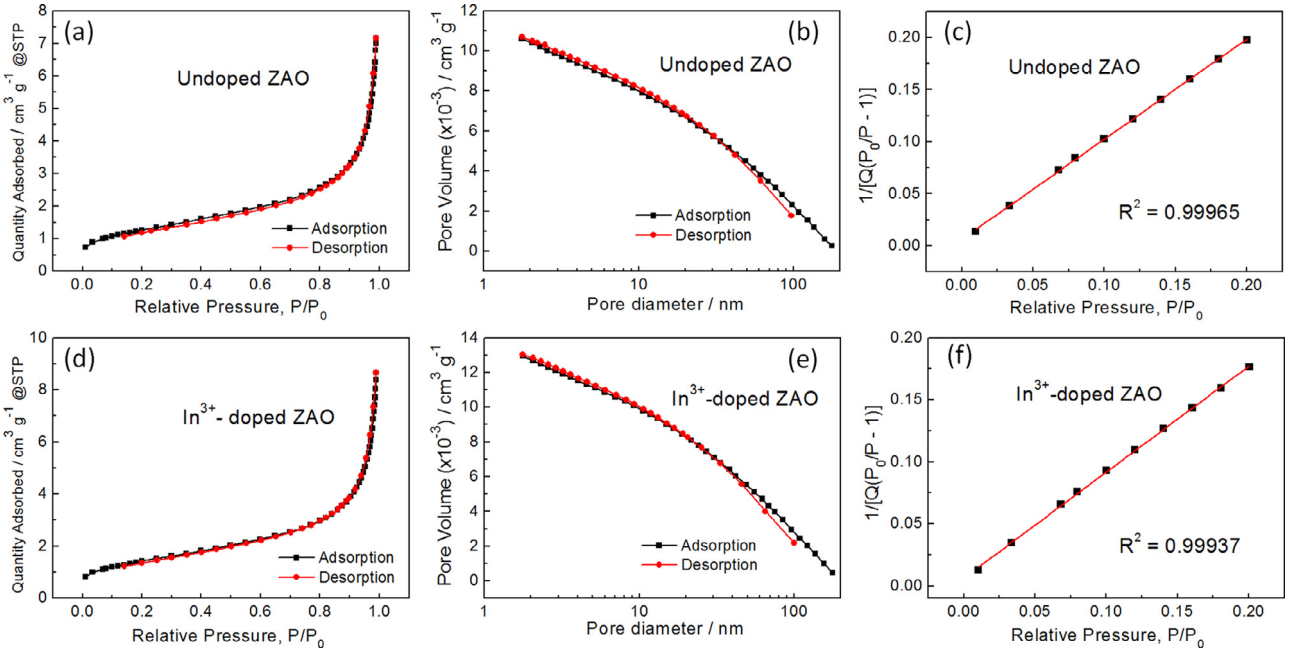

Fig. 6. (a, d) N_2 adsorption/desorption isotherm curves, (b,e) linear multipoint BET plots for nitrogen adsorption, (c,f) pore size distribution curves for undoped and In^{3+}-doped ZAO, respectively.

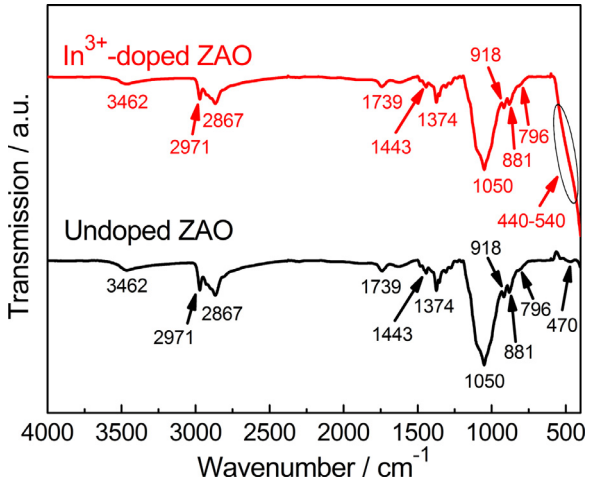

Fig. 7. FTIR spectra of undoped and In^{3+}-doped ZAO.

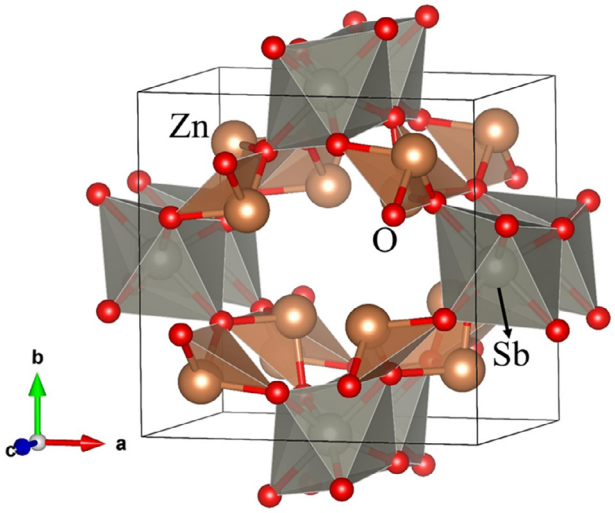

Fig. 8. Crystalline structure of undoped $ZnSb_2O_4$. The Sb distorted octahedra are shaded. The primitive unit cell is also shown.

$c = 5.9210$ Å (JCPDS no. 088-2118). We found that $ZnSb_2O_4$ is a direct band gap material with the band gap of 2.74 eV at Γ point in the Brillouin zone. The calculated band gap using semi-local or local functional such as GGA is well known to be significantly smaller than the measured value. However, the relative stability and major electrical behavior of the In impurities should remain valid. This was tested in our previous DFT calculations of point defects in metal oxides [62].

Our calculated formation energies of In impurities, including In substituted for Sb (In_{Sb}), In substituted for Zn (In_{Zn}), and In at interstitial site (In_i) for the O-poor, intermediate and O-rich conditions are shown in Fig. 9. It is found that In_{Sb} is stable in the neutral, 1− and 2− charge states, acting as double acceptor, which is consistent with the fact that In atom has two valence electrons fewer than Sb. On the other hand, In atom has an extra valence electron when substituted for Zn; thus In_{Zn} exclusively occurs in 1+ charge state for all Fermi-level positions in the band gap, acting as a shallow donor. For In_i, it can donate three valence electrons to neighboring host atoms and occurs in the neutral, 1+ and 3+ charge states, acting as a triple donor. Figs. 9(a-c) show that In_{Sb} has relatively low formation energy for almost the entire range of the Fermi level for all growth conditions. This is possibly because the ionic radii of $In^{3+}$and Sb^{3+} are almost identical, thereby costing small energy for In_{Sb} formation. Besides, for the experimental growth condition (Fig. 9(b)), In_{Sb} has low formation energy and is energetically favorable compared to other In impurities in *p*-type $ZnSb_2O_4$ (in our case), in which the Fermi level lies near the VBM. This indicates that In_{Sb} will form readily during the doping process and its concentration is relatively high.

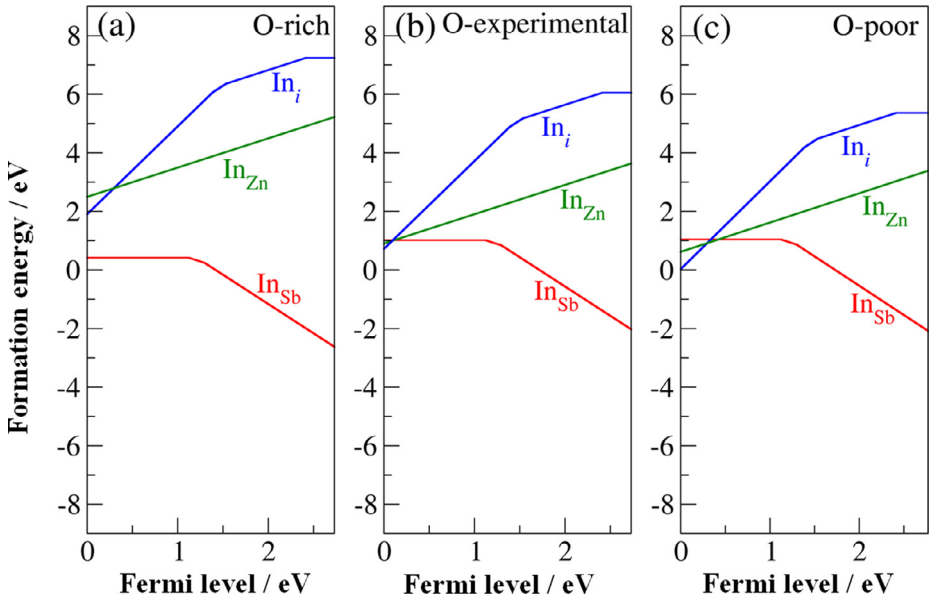

Fig. 9. Formation energies of In impurities as a function of Fermi level ranging from 0 to the calculated band gap of 2.7 eV under (a) O-rich (b) experimental, and (c) O-poor growth conditions. The slope of the line indicates the charge states of the defects.

3.7. Electrochemical measurement

3.7.1. CV characteristics and specific capacitance measurement

The CV characteristics of the undoped and In^{3+}-doped ZAO electrodes at various scan rates (10, 30, 50, 70, and 100 mV s^{-1}) are shown in Figs. 10(a–b), respectively, to compare the electrochemical performances of ion insertion/removal exchange process in the electrodes. The CV scan was performed with a linear potential sweep from -1.0 to + 1.0 V vs. Ag/AgCl and had almost identical redox peaks, suggesting similar electrocatalytic activity for sulfur ion reduction [63,64] and confirming the stable capacitive behavior of the undoped and In^{3+}-doped ZAO electrodes [65]. The asymmetric anodic and cathodic peaks highlight the quasi-reversible charge storage mechanism based on the electrochemical reaction for the S^{2-}insertion/extraction process at the ZAO surface as follows:

$$ZnSb_2O_4 + xS^{2-} \leftrightarrow ZnSb_2O_4S_x + 2xe^- \quad (5)$$

The CV curves of the undoped and In^{3+}-doped electrodes showed a typical Faradic pseudocapacitance behavior from the charge propagation with reversibility in the two pairs of redox response at various scan rates [66]. This was related to the intercalation and deintercalation effects (insertion/removal processes) of disulfide ions from the polysulfide electrolyte into the undoped or In^{3+}-doped ZAO electrode [67]. However, it can be observed that at a lower scan rate, the electrolyte ions have sufficient time to contact the outer and inner active sites of the ZAO mesoporous, which lead a large number of charge accumulation correspond to high specific capacitance value. Meanwhile, the increasing scan rates are attributed to the increase in peak current, implying that the slowing down of processes of ion diffusion or interfacial charge transfer between electrolyte and electrode interfaces as well as reduced numbers of charge accretions on the outer capacitive surface of the electrode material [68-70].

The specific capacitance (C_s) values were calculated from the average current value (I_{avg}) in the CV curves as an equation (6) [71,72]:

$$C_s = \frac{I_{avg}\Delta U}{3.6 \times mV} \quad (6)$$

where ΔU is the operating potential window, m is the weight of active materials (m = 0.0011 ± 0.0001 g with dimensions of 10 mm × 10 mm × 5 μm and 10 mm × 10 mm × 8 μm for the undoped and In^{3+}-doped ZAO electrodes, respectively), and V is the potential scan rate. The C_s plots are displayed in Fig. 10(c). The maximum C_s recorded was 470 mAh g^{-1} at the scan rate of 10 mV s^{-1} for the In^{3+}-doped ZAO electrode, compared to the undoped ZAO electrode (434 mAh g^{-1}). The reduction C_s value was observed to 77 mAh g^{-1} for the In^{3+}-doped ZAO electrode, with the higher scan rate of 100 mV s^{-1}, while the C_s value of 57 mAh g^{-1} was yielded for the undoped ZAO electrode. The higher C_s after In^{3+} doping can be attributed to two potential reasons: (i) indium affects to specific surface area for the ZAO mesoporous; and (ii) the minimal aggregation effect of the nanoscale regime in the ZAO mesoporous [37]. Thus, these will improve its capacity as more sulfur ions from the electrolyte can migrate and diffuse easily between the structures to access the active sites in the ZAO structure [37], resulting in improved conductivity and enhanced capacitor characteristics for the ZAO electrode [26].

3.7.2. Specific power density (PD) and energy density (ED)

The specific PD and ED were respectively calculated based on Equations (7) and (8) [73]:

$$PD = \frac{C_S(\Delta V)s}{2} \quad (7)$$

$$ED = \frac{C_S(\Delta V)^2}{2} \quad (8)$$

The Ragone plot of specific power density (PD) and energy density (ED) for the undoped and In^{3+}-doped ZAO electrodes was performed in Fig. 10(d). The results confirm that after In^{3+} doping, PD reached to 13.92 kW kg^{-1} at the ED equal to 77.34 Wh kg^{-1}, which are greater than those of the undoped electrode (PD = 10.24 kW kg^{-1} at ED = 56.87 Wh kg^{-1}). The In^{3+}-doped ZAO electrode still retains 8.45 kW kg^{-1} at 470 Wh kg^{-1}, compared to the undoped electrode (PD = 7.82 kW kg^{-1} at ED = 434.33 Wh kg^{-1}). It can also be further demonstrated that the In^{3+} doping may improve the electrochemical and energy storage performance of the ZAO electrode.

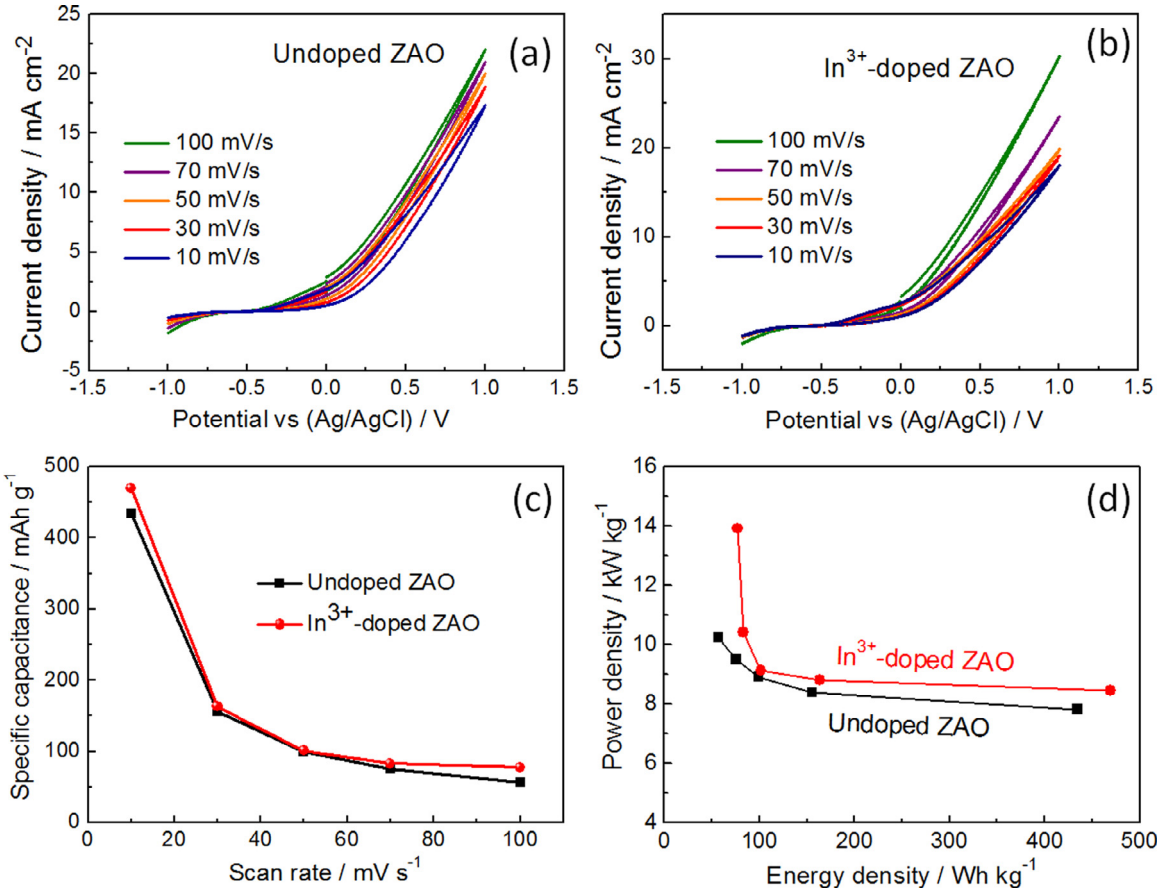

Fig. 10. CV characteristics with various scan rates of (a) undoped and (b) In^{3+}-doped ZAO. (c) specific capacitance vs. scan rate and (d) power density as a function of energy density of undoped and In^{3+}-doped ZAO.

3.7.3. Determination of outer surface and total capacitive charge

The outer surface capacitive charge and total capacitive charge can be further calculated by the Trasatti method, as shown in Figs. 11(a–b), respectively. The charge stored on the outer surface of the undoped and In^{3+}- doped ZAO electrodes (Fig. 11(a)) can be determined from the intercept of linear plot of specific capacitance vs. (scan rate)$^{-1/2}$ based on Equation (9) [74]:

$$Q(V) = Q_{out} + kV^{-1/2} \quad (9)$$

where V is the potential scan rate, Q_{out} is the charge stored at the outer surface and k is a constant. The values of charge stored at the outer surface of undoped and In^{3+}-doped ZAO electrodes are 143 and 147 mAh g^{-1}, respectively. The linear region in Fig. 11(a) indicates a limited diffusion process [7]. Consequently, the total capacitive charge (Q_{total}) (Fig. 11(b)) can be yielded from the intercept of linear plot of (specific capacitance)$^{-1}$ vs. (scan rate)$^{1/2}$ based on Equation (10) [75]:

$$\frac{1}{Q(V)} = \frac{1}{Q_{total}} + kV^{1/2} \quad (10)$$

The value of the Q_{total} is found to be 188 and 366 mAh g^{-1} for the undoped and In^{3+}-doped ZAO electrodes, respectively. The bar graph plotted in Fig. 11(c) represents the total capacitive charge and the outer surface capacitive charge. The difference between the obtained total capacitive charge and the outer surface capacitive charge can give the value of the inner surface capacitive charge [7,16]. All parameter values are listed in Table 2. It is clear that the larger inner surface capacitive charge was obtained due to the diffusion-controlled redox capacity increased with increasing specific surface area in the inner active sites by the influence of In^{3+} doping in the ZAO mesoporous thin film [16], suggesting that the charge storage mechanism is strongly dependent upon the adsorption/desorption process rather than the capacitive process [75,76]. Besides, greater porosity in the inner active sites and heteroatom doping can play a crucial role in enhancing the electrochemical property. In addition, external impacts on the electrochemical and energy storage mechanism were also included, for instance the higher kinetic rate, ion mobility, charge transfer resistance, and electrode conductivity [7,77].

3.7.4. The charge storage mechanism determined by power law fitting

To study the charge storage mechanism of the undoped and In^{3+}-doped ZAO electrodes the power law $i = aV^n$ can be used, where 'a' and 'n' are adjustable parameters and V is the scan rate. The total CV current is the sum of non-Faradic capacitive current and adsorptions/desorption currents. The n value can be determined by the slope of the plot of log i vs. log V and varied from zero to one. The value of $n = 0$ is indicated for a pure resistor, $n = 0.5$ for ideal diffusion control process and $n = 1.0$ for adsorption control of ideal capacitive response or non-Faradic process [70]. Logarithmic values of total CV currents were correlated with the logarithmic values of scan rate and a linear fit is presented in Fig. 11(d). The n value of the undoped ZAO electrode is found to be 0.218, which then increased to 0.635 after In^{3+} doping in the ZAO electrode. This result confirms that the dominant diffusion-controlled redox reaction was expected in the present study [16]. However, it can be noticed that the red dots of the In^{3+}-doped ZAO differs from linearity at high scan rates due to the disparity in charge storage for the two different mechanisms (surface capacitive effects and diffusion-controlled insertion mechanisms) be-

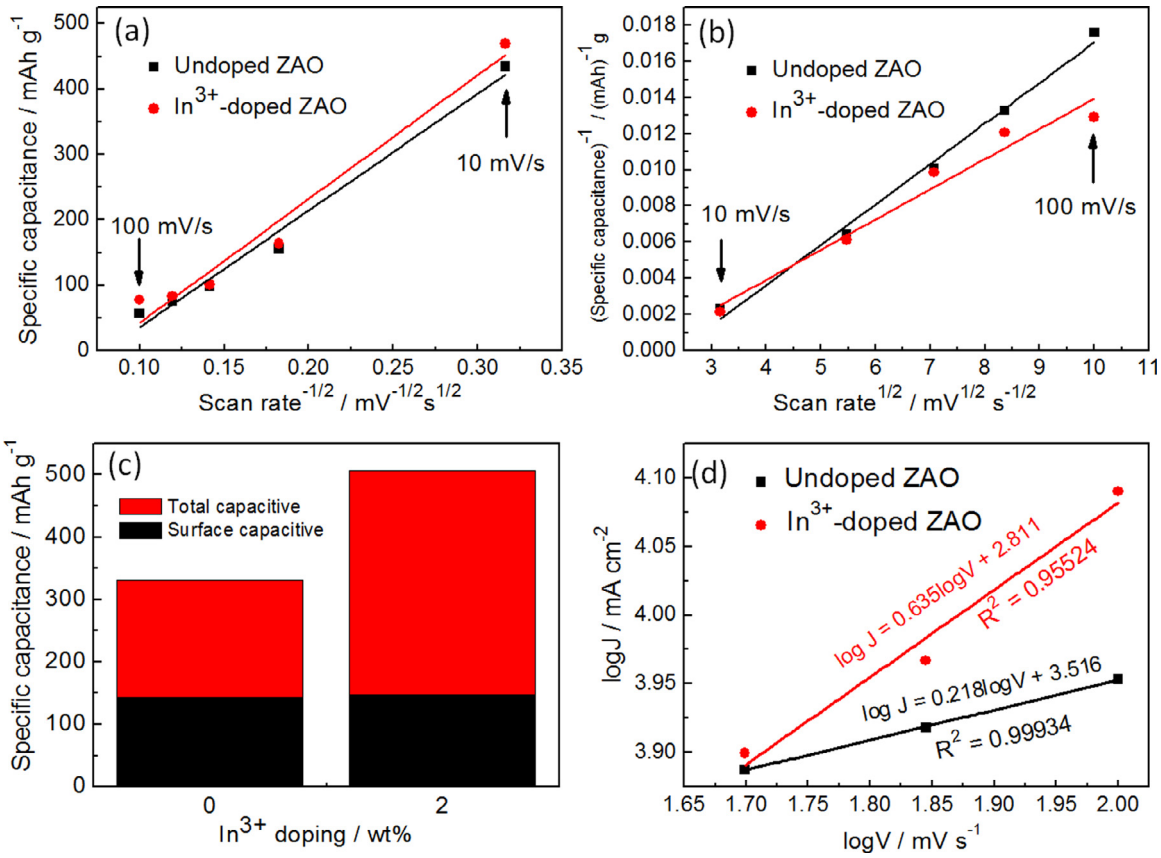

Fig. 11. Trasatti method for (a) a plot of specific capacitance vs. (scan rate)$^{-1/2}$ for the outer surface charge storage determination, (b) a plot of the reciprocal of specific capacitance vs. (scan rate)$^{1/2}$ for the total charge storage determination, (c) the contribution of surface capacitive and total capacitive, and (d) plot of log *I* vs. log *V* for the value of *n* determination.

Table 2
Parameter values derived from cyclic voltammetry and electrochemical impedance spectroscopy

Electrode	Outer surface capacitive charge / mAh g^{-1}	Total capacitive charge / mAh g^{-1}	Inner surface capacitive charge / mAh g^{-1}	R_s / Ω	R_{ct} / Ω	D / cm^2 s^{-1}	μ / cm^2 V^{-1} s^{-1}
Undoped ZAO	143	188	45	31.92	147.3	6.32×10^{-4}	268.26×10^{-4}
In^{3+}-doped ZAO	147	360	213	15.18	135.2	9.84×10^{-4}	417.67×10^{-4}

comes more pronounced at high scan rates because of the rapid charge and discharge characteristics corresponded with capacitive processes. This will be caused by uncompensated ohmic drops and kinetic irreversible redox transitions according to the lower internal resistance of ZAO thin films after In^{3+} doping [78,79].

3.7.5. Electrochemical impedance spectroscopy (EIS)

EIS was used to analyze ionic and electron transport behavior into the electrodes, with the results shown in Fig. 12(a). Generally, the impedance spectrum shows three semicircles at the high, middle, and low frequency regions. From the result, the Nyquist plot clearly shows a semi-circle in the mid-frequency region, but the high frequency semi-circle is not observed in both the undoped and In^{3+}-doped ZAO electrodes. The intercept of the semicircle on the *x*-axis of the Nyquist plot at the high frequency region denotes equivalent series resistance (ESR, R_s) of the electrode, denoted from the internal resistance of electrode plus ionic electrolyte resistance and resistances of all intrinsic or contacts in the electrochemical cell system [7,74]. The lower R_s value in Table 2 was yielded in the In^{3+}-doped ZAO electrode. This could be explained by the penetration of indium into the ZAO electrode during the synthesis, which resulted in rapid ion transport between the electrolyte and ZAO electrode material. Meanwhile, the mid-frequency region arc represents the charge transfer resistance (R_{ct}) in parallel with the constant phase element (CPE1), which actually reflects double layer capacitance effects at the electrode/electrolyte interface. R_{ct} is also known as faradaic resistance, which was obtained from the intercept of the semicircle on the real horizontal axis (Z_{re}) of the mid-frequency region [73]. A smaller semicircle for In^{3+}-doped ZAO electrode demonstrates the lower R_{ct} value of the electrode (see in Table 2). The bode phase plot is displayed in Fig. 12(b) and the phase angles of 36.62° and 47.42° were indicated at the low frequency of 79.43 and 158.49 Hz for undoped and In^{3+}-doped ZAO, respectively, which represents the capacitive behavior of the ZAO material [7]. The transitions between the high and low frequency region are known as the knee frequency (f_{knee}) or called onset frequency [80,81]. The faster charging and discharging behavior can be accomplished at higher f_{knee} and corresponding to the higher rate capability and shorter the relaxation time [7]. The f_{knee} for undoped ZAO was investigated at 10,000 Hz, compared with the higher f_{knee} of 12,589 Hz after In^{3+} doping. The relaxation time (τ) can be calculated based on the knee frequency by $\tau = 1/f_{knee}$ [82] and the values are 0.1 and 0.08 ms, respectively. This shows that the relaxation time decreased when indium atom

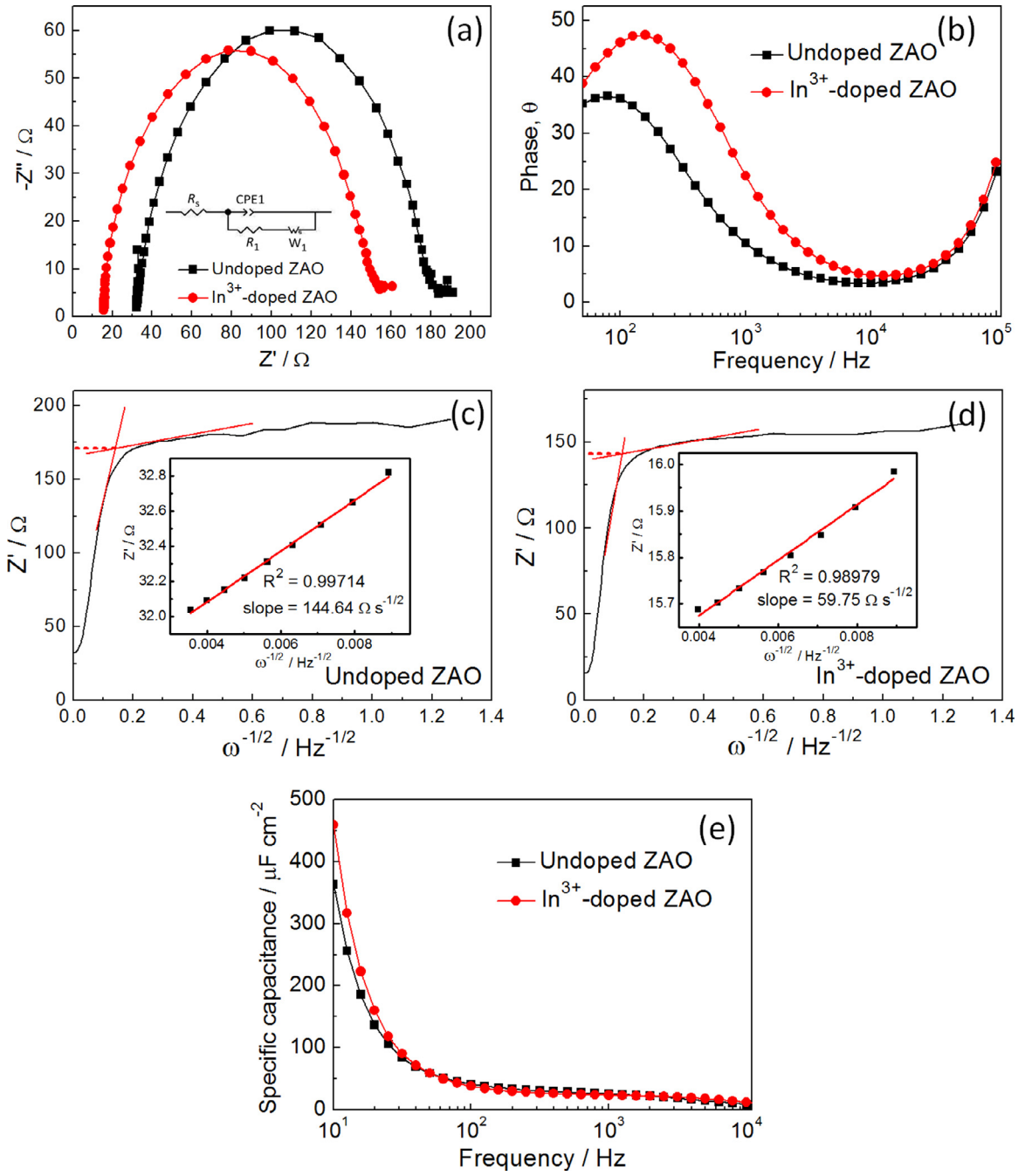

Fig. 12. (a) Nyquist plot and its equivalent circuit (inset), (b) Bode phase plot, (c,d) plots of real impedance (Z') and $\omega^{-1/2}$ (inset: slope of Z' and $\omega^{-1/2}$ for the electrolyte ion diffusion resistance), and (e) specific capacitance vs. frequency for undoped and In^{3+}-doped ZAO.

was incorporated in the ZAO structure. It also refers to the faster charge transfer and better power delivering ability of the electrode [83]. The results of the present study are similar to those of Shanmugavani et al. for pseudocapacitor based on the $ZnFe_2O_4$ NPs treated with $Ni(OH)_2$ [82]. In Figs. 12(c–d), the intercepts of horizontal dash lines on the real part of the impedance (Z') obtained from the Warburg diffusion process, which are equal to 171 and 143 Ω for undoped and In^{3+}-doped ZAO, respectively. The lower Z' value corresponding to a smaller semicircular recombination arc for the In^{3+}-doped ZAO electrode, attributing to the barrier layer is reduced, and the finite diffusion length was increased. The kinetics reaction of charge transfer at electrode/electrolyte interface can be indicated by the electrolyte ion diffusion resistance (σ) as the faster kinetics reaction defined by a lower σ value according to Equation (11) [84]:

$$Z_w = \sigma \omega^{-\frac{1}{2}} (1 - j) \tag{11}$$

The slopes of Z' against the reciprocal of the square root of frequency ($\omega^{-\frac{1}{2}}$) are shown in the inset of Figs. 12(c–d) and the obtained σ value decreased from 144.64 Ω $s^{-1/2}$ for the undoped ZAO electrode to 59.75 Ω $s^{-1/2}$ for the In^{3+}-doped ZAO electrode. This could be related to the faster reaction kinetics and better diffusion of charge transfer at electrode/electrolyte interface. Moreover, the Faradaic redox process also occurred at the surface of the In^{3+}-incorporated electrode with a yielded higher exchange current density. Consequently, the diffusion coefficient can also be cal-

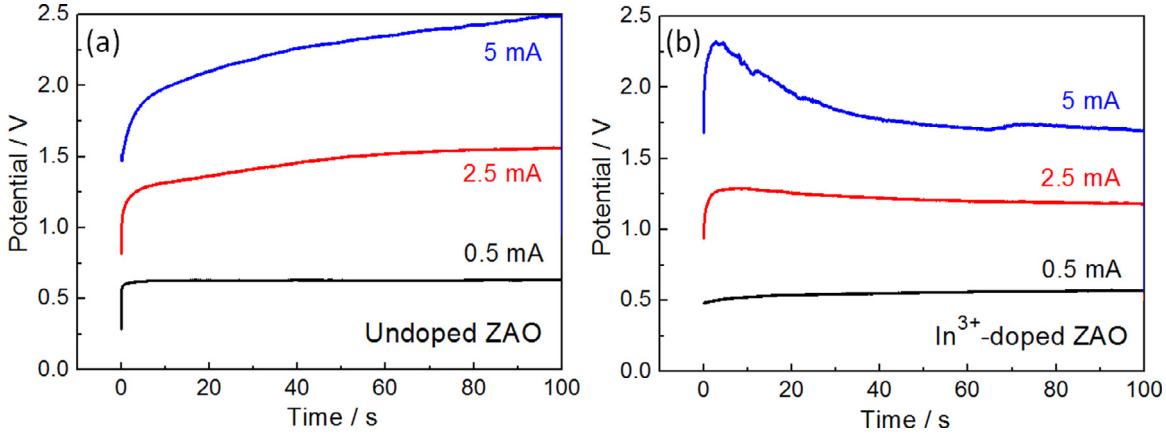

Fig. 13. Chronopotentiometry measurement with various applied currents of (a) undoped and (b) In^{3+}-doped ZAO.

culated using Equation (12) [7]:

$$\sigma = \frac{RT}{n^2F^2A\sqrt{2}}\left(\frac{1}{D^{1/2}C^*}\right) \quad (12)$$

where R is universal gas constant, T is temperature (298 K), n is charge transfer number (here considering n =1), F represents the Faraday constant (96,485.3 C mol^{-1}), A is referred to as an area of the electrode (A = 10 mm^2), D is diffusion coefficient, and C^* is concentration of sulfur atoms in the polysulfide electrolyte and CuS counter electrode (0.00325 mol cm^{-3}). Then, the obtained value of D is related to the ionic mobility (μ) and can be further calculated based on the Nerst-Einstein equation, as in Equation (13) [85]:

$$\mu = \frac{eD}{K_BT} \quad (13)$$

where e is the charge value of electron, K_B is the Boltzmann constant and T is the absolute temperature (273.15 K). It can be seen that the D and μ values (listed in Table 2) increased for the In^{3+}-doped ZAO electrode. These enhancements correspond to an improved ion storage capacity that allows larger ionic concentration for the insertion/extraction into/from the ZAO material. Thus, a larger ion diffusion coefficient indicates faster movement of S^{2-} and Na^+ ions to the working electrode and counter electrode, respectively, corresponding to a shortened relaxation time of the charging and discharging states and effective diffusion path [86].

Moreover, the capacitance (C) was calculated using the equation $C = -1/2\pi fZ''$, where f is the frequency in Hz, and Z'' is the imaginary part of the impedance spectrum [87]. The areal specific capacitance ($C_s = C/S$ with S = 10 mm^2) is plotted in Fig. 12(e). As the frequency decreased from 10^4 to 10 Hz, C_s increased for both electrodes, while the ZAO electrode with In^{3+} performed a higher C_s in the low-frequency region (10 – 100 Hz). This could be attributed to more electrons diffused into the In^{3+}-incorporated ZAO structure, with a lower barrier layer and charge transfer resistance at the interface. Subsequently, the capacitance of the electrode was enhanced, with a higher electrical conductivity by the introduction of In^{3+} ions. This behavior is similar to the previous report on the co-incorporation of Mn^{2+} and Cu^{2+} ions in the Sn_2S_3 electrode for electrochemical devices [88] and confirms the increased energy storage performance in the fabricated ZAO electrode, since an electron transport pathway was shortened and faster carrier diffusion was also induced [89].

3.7.6. Chronopotentiometry (CP)

In Figs. 13(a–b), CP characteristics for undoped and In^{3+}-doped ZAO electrodes are presented with the dynamic voltage response in time and various applied constant current (0.5, 2.5, and 5 mA), respectively. The chronopotentiometric responses (Fig. 13(a)) in the potential were stepped from the initial potential to the finite potential in each applied constant current condition. The spectra were recorded with time to identify transport limitations, charge exchange ability, chemical reaction mechanisms, and the rate of oxidation kinetics [90,91]. With the higher applied current through the electrode, the potential curve increases from the open-circuit potential (OCP) and continues to increase with time to reach a value at which S^{2-} ions diffusing into the electrode through the oxidation process. This leads a reduction of electrical resistance with time in the electrode, owing to the faster diffusion of the S^{2-} ions. At the applied current of 0.5 – 2.5 mA, the steady-state potential reached the maximum value, which was approached by a steady increase after the transition time [91]. However, after In^{3+} doping in the ZAO electrode in Fig. 13(b), the performance of the chronopotentiometric responses are similar to the previous study of Wilhelm et al. [91] and explains that the characteristic response curves are observed with maximum or overshoot of the electric potential at the applied current from 2.5 to 5 mA. This applied current range is the limiting current for the electrode with In^{3+} doping. The depletion process at the interface occurred, which was induced to enable a larger number of faster ion exchange in the bipolar junction (i.e., working and CE electrodes). At this applied current range, the initial increase of the potential was observed due to ion depletion in the diffusion layer of the electrode and additional ion exchange was performed based on the reduction of the charge transfer resistance at the electrode/electrolyte interfaces. Next, the ion leakage across the electrode is related to the limiting current, observed by the reduction of potential with time. This result indicates a negative slope, extended over longer time period with higher current densities. The negative slope of the potential with time indicates the self-discharge characteristic of the electrode. At that time, the diffusion processes in the electrode interface relaxed and produced ions to such an extent recombination reaction in the bipolar junction. The self-discharge characteristic in Fig. 13(b) is observed at a longer range of time (also referred to as discharging time) for a higher current density because the higher ion dissociation was produced [90,91].

3.7.7. Charge/discharge characteristics

The charge and discharge characteristics with various galvanostatic charge and discharge cycles are shown in Figs. 14(a–b) for undoped and In^{3+}-doped ZAO electrodes, respectively to observe the cycling performance and their stability. Both electrodes were performed under 0 to 150 cycles with a scan rate of 0.1 V s^{-1} and the specific capacitance of each cycle for charge/discharge from the

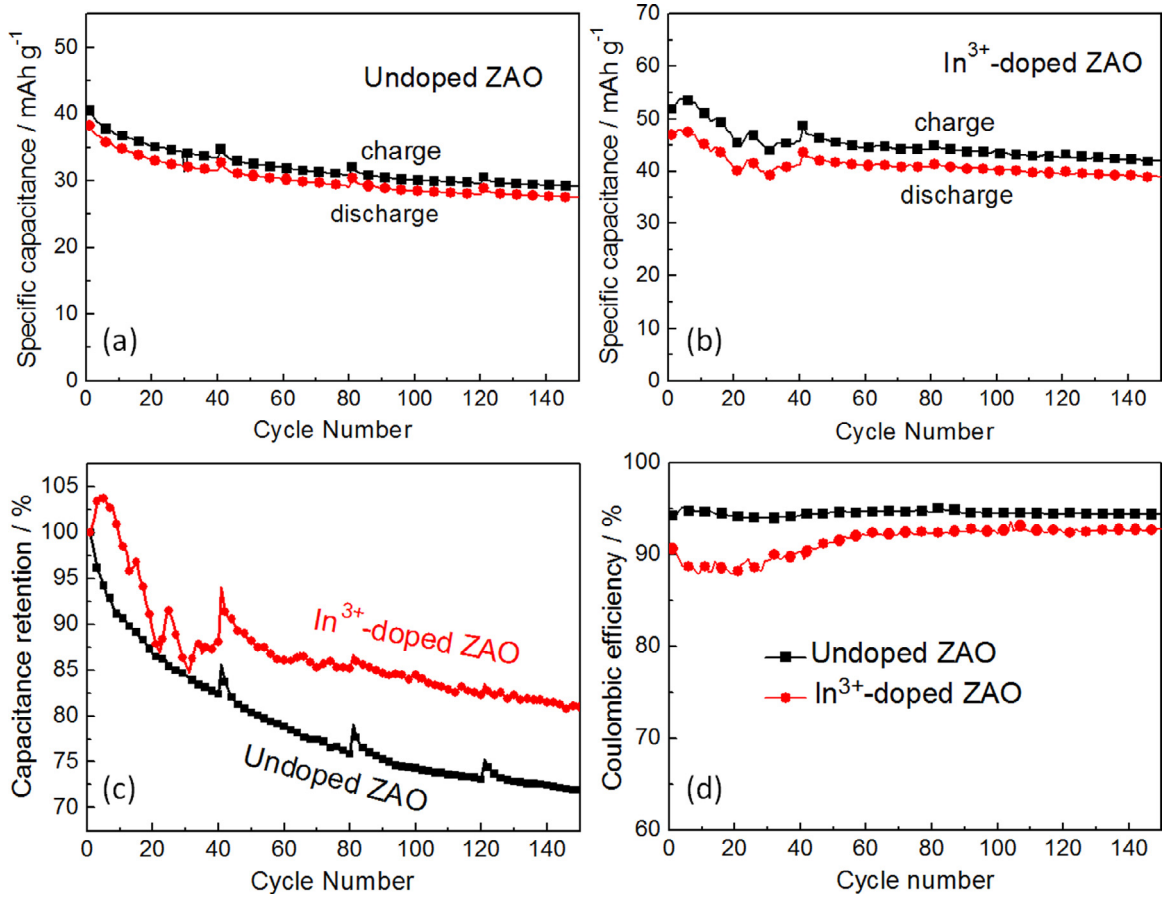

Fig. 14. (a,b) specific capacitance, (c) capacitance retention, and (d) coulombic efficiency as a function of cycle number of undoped and In^{3+}-doped ZAO.

CV curves was then calculated. The highest C_s values of the charge and discharge cycles for the undoped electrode was respectively ~ 40 and 38 mAh g^{-1} (Fig. 14(a)) with average C_s values of ~32 and 30 mAh g^{-1}. The increased C_s in the charge and discharge curves was performed after In^{3+} doping in the ZAO electrode and the highest C_s values of ~ 54 and 48 mAh g^{-1} (Fig. 14(b)) with average C_s values of ~ 45 and 41 mAh g^{-1} were respectively obtained. Yet the In^{3+}-doped ZAO electrode had the higher discharge process ~ 9–11%, compared to the lower discharge process of the undoped ZAO electrode of ~ 5–6%. In addition, the largest capacitance retention of ~ 104% with an average value of ~ 87 % was found with the In^{3+}-doped ZAO electrode, compared with an average value for the undoped ZAO electrode (~ 79%) (Fig. 14(c)). The larger capacitance retention possesses a long-term stability of the electrochemical performance, which is another important issue in an active electrode for the practical application of supercapacitors. From Fig. 14(d), the average lower coulombic efficiency of ~ 91% for the In^{3+}-doped ZAO electrode reduced from ~94% by the undoped ZAO electrode due to the self-discharge process (explained in Section 3.7.6). The additional explanation of a self-discharge process for the lower coulombic efficiency can be explained by Knap et al. [92] and is related to the polysulfide shuttle mechanism [93], which is caused by the diffusion of soluble high-order polysulfideions (S_8^{2-}, S_6^{2-}, S_4^{2-}) in the electrolyte from the sulfur electrode to the ZAO electrode. Then, the reversible process also occurred as the high-order polysulfides were reduced to low-order polysulfides and the ions could be diffused back to the sulfur electrode (CE). Meanwhile, the fast kinematics and diffusion process of ion transport induced by indium may lead to electrode material degradation, which also resulted in the low coulombic efficiency of the fabricated material [7].

4. Conclusion

We demonstrated the simple synthesis of undoped and In^{3+}-doped multi-phase ZAO thin films from a wet chemical solution for a pseudocapacitor application. Based on electronic structure calculations, the In^{3+}-doped $ZnSb_2O_4$ behaves similar to a weak *p*-type semiconductor with the lower-than-band gap optical absorption and performs greater charge storage performance diffused into the In^{3+}-incorporated ZAO structure. This leads to obtaining a lower barrier layer and charge transfer resistance at the interface. The 1.4 fold increment of energy density (from 56.87 to 77.34 Wh kg^{-1}) and power density (from 10.24 to 13.92 kW kg^{-1}) was yielded after In^{3+} doping. Thus, the specific capacitance of the electrode also enhanced from 434 mAh g^{-1} to 470 mAh g^{-1} at the scan rate of 10 mV s^{-1}. In addition, the largest capacitance retention of ~ 104% with an average value of ~ 87 % was found for the In^{3+}-doped ZAO electrode. However, the average lower coulombic efficiency of ~ 91% for the In^{3+}-doped ZAO electrode was performed due to the self-discharge process and the diffusion of soluble high-order polysulfide ions. Furthermore, ion transport induced by indium may lead to electrode material degradation due to the fast kinematics and diffusion process in the electrode interfaces, which also resulted in the low coulombic efficiency of the fabricated material.

Authors' contribution

Duanghatai Raknual: Conceptualization, Methodology, Formal analysis, Investigation, Data Curation.

Supparat Charoenphon: Conceptualization, Methodology, Formal analysis, Data Curation.

Pakpoom Reunchan: Conceptualization, Methodology, Validation, Formal analysis,

Writing - Original Draft Preparation, Writing - Review& Editing Preparation, Funding acquisition.

Auttasit Tubtimtae: Conceptualization, Methodology, Validation, Formal analysis, Investigation, Resources, Data Curation, Writing - Original Draft Preparation, Writing - Review& Editing Preparation, Project administration, Funding acquisition.

Declaration of Competing Interest

The authors declare no known competing financial interests or personal relationships that could have influenced the work reported in this paper.

Acknowledgment

D.R. acknowledges the financial support received from the Student Development Fund and the Research Promotion and Technology Transfer Center (RPTTC) under the Faculty of Liberal Arts and Science, Kasetsart University, Kamphaeng Saen Campus, Thailand (Grant no. 205/2563). S.C. is funded by Kasetsart University through the Graduate School Fellowship program. The authors would also like to thank Dr. Veeramol Vailikhit and Dr. Panitat Hasin for their support with the experimental set up of the CV and EIS measurements, respectively.

Supplementary materials

Supplementary material associated with this article can be found, in the online version, at doi:10.1016/j.electacta.2021.138773.

References

[1] K. Wua, J. Zhaoa, X. Zhanga, H. Zhou, M. Wu, Hierarchical mesoporous MoO_2 sphere as highly effective supercapacitor electrode, J. Taiwan Inst. Chem. Eng. 102 (2019) 212–217.
[2] R.C. Ambare, P. Shinde, U.T. Nakate, B.J. Lokhande, R.S. Mane, Sprayed bismuth oxide interconnected nanoplate supercapacitor electrode materials, Appl. Surf. Sci. 453 (2018) 214–219.
[3] M. Szkoda, Z. Zarach, K. Trzcínski, G. Trykowski, A.P. Nowak, An easy and ecological method of obtaining hydrated and non-crystalline WO_{3-x} for application in supercapacitors, Materials 13 (2020) 1925.
[4] J. Sribenjawan, D. Raknual, V. Vailikhit, N. Kitisripanya, A. Tubtimtae, Facile synthesis of copper-antimony-sulfide nanostructures on WO_3 electrodes: Investigation of electrochemical performance, Mater. Lett. 245 (2019) 126–129.
[5] D. Majumdar, M. Mandal, S.K. Bhattacharya, Review on V_2O_5 and its carbon-based nanocomposites for supercapacitor applications, Chem. Electro. Chem. 6 (2019) 1623–1648.
[6] Y. Liu, X. Cao, D. Jiang, D. Jia, J. Liu, Hierarchical CuO nanorod arrays: In situ generated on threedimensional copper foam via cyclic voltammetry oxidation for high-performance supercapacitors, J. Mater. Chem. A. 6 (2018) 10474–10483.
[7] S.P. Gupta, S.W. Gosavi, D.J. Late, Q. Qiao, P.S. Walke, Temperature driven high--performance pseudocapacitor of carbon nano-onions supported urchin like structures of a-MnO_2 nanorods, Electrochimica Acta 354 (2020) 136626.
[8] V. Augustyn, P. Simon, B. Dunn, Pseudocapacitive oxide materials for high-rate electrochemical energy storage, Energy Environ. Sci. 7 (2014) 1597–1614.
[9] S. Wang, Y. Teng, X. Liu, D. Yu, Y. Meng, Y. Wu, S. Sun, X. Zhao, X. Liu, Facile synthesis of mesoporous $ZnCo_2O_4$ nanowire arrays and nanosheet arrays directly grown on nickel foam for high-performance supercapacitors, Inorg. Chem. Commun. 101 (2019) 16–22.
[10] G. Gao, H.B. Wu, S. Ding, L.M. Liu, X.W. Lou, Hierarchical $NiCo_2O_4$ nanosheets grown on Ni nanofoam as high-performance electrodes for supercapacitors, Small 11 (2015) 804–808.
[11] Z. Yu, B. Duong, D. Abbitt, J. Thomas, Highly ordered MnO_2 nanopillars for enhanced supercapacitor performance, Adv. Mater. 25 (2013) 3302–3306.
[12] T. Brousse, D. Bélanger, J.W. Long, To be or not to be pseudocapacitive? J. Electrochem. Soc. 162 (2015) A5185–A5189.
[13] P. Simon, Y. Gogotsi, B. Dunn, Where do batteries end and supercapacitors begin? Science Magazine 343 (2014) 1210–1211.
[14] S. Gupta, V. Patil, N. Tarwal, S. Bhame, S. Gosavi, I. Mulla, D. Late, S. Suryavanshi, P. Walke, Enhanced energy density and stability of self-assembled cauliflower of Pd doped monoclinic WO_3 nanostructure supercapacitor, Mater. Chem. Phys. 225 (2019) 192–199.
[15] W. Qian, F. Sun, Y. Xu, L. Qiu, C. Liu, S. Wang, F. Yan, Human hair-derived carbon flakes for electrochemical supercapacitors, Energy Environ. Sci. 7 (2014) 379–386.
[16] A.D. Deshmukh, A.R. Urade, A.P. Nanwani, K.A. Deshmukh, D.R. Peshwe, P. Sivaraman, S.J. Dhoble, B.K. Gupta, ACS Omega 3 (2018) 7204–7213.
[17] M.A. Alim, S. Li, F. Liu, P. Cheng, Electrical barriers in the ZnO varistor grain boundaries, Phys. Status Solidi A 203 (2006) 410–427.
[18] J. Cheng, Y. Lu, K. Qiu, H. Yan, X. Hou, J. Xu, L. Han, X. Liu, J.K. Kim, Y. Luo, Mesoporous $ZnCo_2O_4$ nanoflakes grown on nickel foam as electrodes for high performance supercapacitors, Phys. Chem. Chem. Phys. 17 (2015) 17016–17022.
[19] S. Battistoa, C. Riga, E.C. Severo, M.A. Mazutti, R.C. Kuhn, A. Gündel, E.L. Foletto, Synthesis of zinc aluminate ($ZnAl_2O_4$) spinel and its application as photocatalyst, Mater. Res. 17 (2014) 734–738.
[20] S.D. Shenoya, P.A. Joyb, M.R. Anantharamana, Effect of mechanical milling on the structural, magnetic and dielectric properties of coprecipitatedultrafine zinc ferrite, J. Magn. Magn. Mater. 269 (2004) 217–226.
[21] S. Peng, Y. Tang, L. Jin, Y. Wang, L. Ma, F. Cao, Comparison of the electro-optical performance of ZnO:Al and ZnO:B thin films derived by sol-gel method, Surf. Coat. Tech. 310 (2017) 251–255.
[22] J.L. Wu, H.Y. Lin, Y.C. Chen, S.Y. Chu, C.C. Chang, C.J. Wu, Y.D. Juang, Effects of ZnO buffer layer on characteristics of ZnO:Ga films grown on flexible substrates: investigation of surface energy, electrical, optical, and structural properties, Ecs J. Solid State Sc. 2 (2013) 115–119.
[23] Z. Mousavi, F. Soofivand, M. Esmaeili-Zare, M. Salavati-Niasari, S. Bagheri, $ZnCr_2O_4$ nanoparticles: facile synthesis,characterization, and photocatalytic properties, Sci. Rep. 6 (2016) 20071.
[24] S. Khalid, F. Saleemi, R. Zia, S. Anjum, F. Bashir, N. Tahir, A. Haq, Crystal development and analysis of zinc-antimony oxide synthesized by solid state synthesis technique, Optik 127 (2016) 10172–10179.
[25] D.W. Zeng, C.S. Xie, M. Dong, R. Jiang, X. Chen, A.H. Wang, J.B. Wang, J. Shi, Spinel-type $ZnSb_2O_4$ nanowires and nanobelts synthesized by an indirect thermal evaporation, Appl. Phys. A 79 (2004) 1865–1868.
[26] M. Balasubramaniam, S. Balakumar, Exploration of electrochemical properties of zinc antimonate nanoparticles as supercapacitor electrode material, Mater. Sci. Semicond. Process 56 (2016) 287–294.
[27] P. Villars, K. Cenzual, R. Gladyshevskii, O. Shcherban, V. Dubenskyy, V. Kuprysyuk, I. Savysyuk, R. Zaremba, in: $ZnSb_2O_4$". Structure Types. Part 11: Space groups (135) P42/mbc–(123) P4/mm, Springer, Berlin Heidelberg, 2012, p. 52.
[28] N. Arunkumar, R. Vijayaraghavan, in: Enhanced photocatalytic activity of nanocrystalline N-doped $ZnSb_2O_6$: role of N doping, cation ordering, particle size and crystallinity, 4, RSC Adv, 2014, pp. 65223–65231.
[29] T. Aoki, Y. Shimizu, A. Miyake, A. Nakamura, Y. Nakanishi, Y. Hatanaka, p–type ZnO layer formation by excimer laser doping, Phys. Stat. Sol 229 (2002) 911–914.
[30] D.W. Zeng, C.S. Xie, M. Dong, R. Jiang, X. Chen, A.H. Wang, J.B. Wang, J. Shi, Spinel-type $ZnSb_2O_4$ nanowires and nanobelts synthesized by an indirect thermal evaporation, Appl. Phys. A 79 (2004) 1865–1868.
[31] D.P. Dutta, A. Ballal, A. Singh, M.H. Fulekar, A.K. Tyagi, Multifunctionality of rare earth doped nano $ZnSb_2O_6$, $CdSb_2O_6$ and $BaSb_2O_6$: photocatalytic properties and white light emission, Dalton Trans 42 (2013) 16887–16897.
[32] M. Balasubramaniam, S. Balakumar, Contribution of tin in electrochemical properties of zinc antimonate nanostructures: An electrode material for supercapacitors, AIP Conf Proc 1942 (2018) 140013.
[33] M. Balasubramaniam, S. Balakumar, On the development of hierarchical nanostructures of graphene-zinc antimonate as inexpensive electrode materials for supercapacitors, Electrochim. Acta 253 (2017) 178–189.
[34] N. Buatong, I.M. Tang, W. Pon-On, The study of metal sulfide as efficient counter electrodes on the performances of CdS/CdSe/ZnS-co-sensitized hierarchical TiO_2 sphere quantum dot solar cells, Nanoscale Res. Lett. 12 (2017) 170.
[35] J.P. Perdew, K. Burke, M. Ernzerhof, Generalized gradient approximation made simple, Phys. Rev. Lett. 77 (1996) 3865–3868.
[36] G. Kresse, J. Furthmüller, Efficiency of *ab-initio* total energy calculations for metals and semiconductors using a plane-wave basis set, Comput. Mater. Sci. 6 (1996) 15–50.
[37] M. Balasubramaniam, S. Balakumar, Ultrasonication-assisted fabrication of hierarchical architectures of copper oxide/zinc antimonate nanocomposites based supercapacitor electrode materials, Ultrasonics - Sonochem. 56 (2019) 337–349.
[38] P. Suttiyarak, S. Buathet, A. Tubtimtae, Undoped and In^{3+}-doped WO_3 electrodes coated with Cu_7Te_4 nanocrystals and Bi_2Te_3 thin films: Investigation of morphological, structural and optical properties, Optik 212 (2020) 164662.
[39] J.U. Brehm, M. Winterer, H. Hahn, Synthesis and local structure of doped nanocrystalline zinc oxides, J. Appl. Phys. 100 (2006) 064311.
[40] E.N.A.A. Armah, M. Egblewogbe, H.A. Koffi, A.A. Yankson, F.K. Ampong, F. Boakye, J.K.A. Amuzu, R.K. Nkum, Solubility of Mn in ZnO crystallites synthesized using solid state techniques, Adv. Nano Res. 3 (2020) 28–39.
[41] P. Suttiyarak, A. Tubtimtae, P-type In^{3+}-doped $Cu_{12}Sb_4S_{13}$ thin films deposited by spray pyrolysis method: Investigation of structural, optical, electrical, and electrocatalytic properties, Appl. Surf. Sci. 527 (2020) 146835.
[42] R.D. Shannon, Revised effective ionic radii and systematic studies of interatomic distances in halides and chalcogenides, Acta Crystallogr. A 32 (1976) 751–767.
[43] G. Singh, S.B. Shrivastava, D. Jain, S. Pandya, T. Shripathi, V. Ganesan, Effect

of indium doping on zinc oxide films prepared by chemical spray pyrolysis technique, Bull. Mater. Sci. 33 (2010) 581–587.
[44] X. Zhang, H. Lee, J.H. Kwon, E.J. Kim, J. Park, Low-concentration indium doping in solution-processed zinc oxide films for thin-film transistors, Materials 10 (2017) 880.
[45] R. Casanova, J. Mendialdua, A. Loaiza-Gil, A. Rodríguez, F. Rueda, Characterization of iron phyllosilicate catalysts by means of kll auger spectra of oxygen, Rev. Latin. Am. Met. Mat. 22 (2002) 78–81.
[46] L. Wang, D. Wang, X.Y. Dong, Z.J. Zhang, X.F. Pei, X.J. Chen, B. Chen, J. Jin, Layered assembly of graphene oxide and Co–Al layered double hydroxide nanosheets as electrode materials for supercapacitors, Chem. Commun. 47 (2011) 3556–3558.
[47] R. Al-Gaashani, S. Radiman, A.R. Daud, N. Tabet, Y. Al-Douri, XPS and optical studies of different morphologies of ZnO nanostructures prepared by microwave methods, Ceram. Inter. 39 (2013) 2283–2292.
[48] R.G. Copperthwaite, O.A. Kunze, J. Lloyd, J.A. Neely, W. Tuma, Surface analysis of InSb by X-ray photoelectron spectroscopy (XPS), Z. Naturforsch. 33a (1978) 523–527.
[49] N.P. Herring, L.S. Panchakarla, M.S. El-Shall, P-type nitrogen-doped ZnO nanostructures with controlled shape and doping level by facile microwave synthesis, Langmuir 30 (2014) 2230–2240.
[50] Z. Zhuang, Q. Peng, J. Liu, X. Wang, Y. Li, Indium hydroxides, oxyhydroxides, and oxides nanocrystals series, Inorg. Chem. 46 (2007) 5179–5187.
[51] H. Mao, D. Zhou, Z. Hashisho, S. Wang, H. Chen, H. Wang, M.J. Lashaki, Microporous activated carbon from pinewood and wheat straw by microwaveassisted KOH treatment for the adsorption of toluene and acetone vapors, RSC Adv. 5 (2015) 36051–36058.
[52] G. Nagaraju, Shivaraj Udayabhanu, S.A. Prashanth, M. Shastri, K.V. Yathish, C. Anupama, D. Rangappa, Electrochemical heavy metal detection, photocatalytic, photoluminescence, biodiesel production and antibacterial activities of Ag–ZnO nanomaterial, Mater. Res. Bull. 94 (2017) 54–63.
[53] J.R. Reddy, G. Ravi, P. Suresh, N.K. Veldurthi, R. Velchuri, M. Vithal, Antimony potassium tartrate, J. Therm. Anal. Calorim. 115 (2014) 1321–1327.
[54] B. Ksapabutr, E. Gulari, S. Wongkasemjit, One-pot synthesis and characterization of novel sodium tris (glycozirconate) and cerium glycolate precursors and their pyrolysis, Mater. Chem. Phys. 83 (2004) 34–42.
[55] S. Bahfenne, R.L. Frost, Vibrational spectroscopic study of the antimonate mineral stibiconite Sb3+Sb25+O6(OH), Spectrosc. Lett. 43 (2010) 486–490.
[56] G.A. Babu, P. Ramasamy, Synthesis, crystal growth and characterization of novel semiorganic nonlinear optical crystal: Dichlorobis(l-proline)zinc(II), Mater. Chem. Phys. 113 (2009) 727–733.
[57] M. Anand, P. Sathyapriya, M. Maruthupandy, A. Hameedha Beevi, Synthesis of chitosan nanoparticles by TPP and their potential mosquito larvicidal application, Front. Lab. Med. 2 (2018) 72–78.
[58] M. Stefanescu, M. Stoia, O. Stefanescu, Thermal and FT-IR study of the hybrid ethylene-glycol–silica matrix, J. Sol-Gel Sci. Techn. 41 (2007) 71–78.
[59] R. Zamiri, A. Rebelo, G. Zamiri, A. Adnani, A. Kuashal, M.S. Belsley, J.M.F. Ferreira, Far-infrared optical constants of ZnO and ZnO/Ag nanostructures, RSC Adv. 4 (2014) 20902–20908.
[60] L.A. Burton, A. Walsh, A photoactive titanate with a stereochemically active Sn lone pair: Electronic and crystal structure of Sn_2TiO_4 from computational chemistry, J. Solid State Chem. 196 (2012) 157–160.
[61] B. Dickens, The bonding in Pb_3O_4 and structural principles in stoichiometric lead oxides, J. Inorg. Nucl. Chem. 27 (1965) 1509–1515.
[62] I. Chatratin, F.P. Sabino, P. Reunchan, S. Limpijumnong, J.B. Varley, C.G. Van de Walle, A. Janotti, Role of point defects in the electrical and optical properties of In_2O_3, Phys. Rev. Mater. 3 (2019) 074604.
[63] Z. Yang, C.Y. Chen, P. Roy, H.T. Chang, Quantum dot sensitized solar cells incorporating nanomaterials, Chem. Commun. (J. Chem. Soc. Sect. D) 47 (2011) 9561–9571.
[64] H.J. Kim, L. Myung-Sik, C.V. Gopi, M. Venkata-Haritha, S.S. Rao, S.K. Kim, Cost effective and morphology controllable PVP based highly efficient CuS counter electrodes for high-efficiency quantum dot-sensitized solar cells, Dalton Trans 44 (2015) 11340–11351.
[65] B.E. Conway, Electrochemical supercapacitors and their complementarity to fuel cells and batteries, Wiley, New York, 2010.
[66] H. Mudila, M.G.H. Zaidi, S. Rana, S. Alam, Comparative electrochemical study of sulphonated polysulphone binded graphene oxide supercapacitor in two electrolytes, Carbon Lett 18 (2016) 43–48.
[67] L.D. Trizio, R. Gaspari, G. Bertoni, I. Kriegel, L. Moretti, F. Scotognella, L. Maserati, Y. Zhang, G.C. Messina, M. Prato, S. Marras, A. Cavalli, L. Manna, $Cu_{3-x}P$ nanocrystals as a material platform for near-infrared plasmonics and cation exchange reactions, Chem. Mater. 27 (2015) 1120–1128.
[68] H.K. Jeong, M. Jin, E.J. Ra, K.Y. Sheem, G.H. Han, S. Arepalli, Y.H. Lee, Enhanced electric double layer capacitance of graphite oxide intercalated by poly (sodium 4-styrensulfonate) with high cycle stability, ACS Nano 4 (2010) 1162–1166.
[69] K.H. An, K.K. Jeon, J.K. Heo, S.C. Lim, D.J. Bae, Y.H. Lee, High-capacitance supercapacitor using a nanocomposite electrode of single-walled carbon nanotube and polypyrrole, J. Electrochem. Soc. 149 (2002) A1058–A1062.
[70] A. Ray, A. Roy, S. Saha, S. Das, Transition metal oxide-based nano-materials for energy storage application, science, technology and advanced application of supercapacitors, IntechOpen (2018) 1–17.
[71] S. Zhang, N. Pan, Supercapacitors performance evaluation, Adv. Energy Mater. 5 (2015) 1401401.
[72] D. Gromadskyi, V. Chervoniuk, S. Kirillov, Cyclic voltammetric study of tin hexacyanoferrate for aqueous battery applications, J. Electrochem. Sci. Eng. 6 (2016) 225–234.
[73] A.K. Samantara, S.C. Sahu, A. Ghosh, B.K. Jena, Sandwiched graphene with nitrogen, sulphur co-doped CQDs: an efficient metal-free material for energy storage and conversion applications, J. Mater. Chem. 3 (2015) 16961–16970.
[74] R. Mohammadi, S. Shahrokhian, In-situ fabrication of nanosheet arrays on copper foil as a new substrate for binder-free high-performance electrochemical supercapacitors, J. Electroanal. Chem. 802 (2017) 48–56.
[75] A. Roy, A. Ray, S. Saha, S. Das, Investigation on energy storage and conversion properties of multifunctional PANI-MWCNT composite, Int. J. Hydrog 43 (2018) 7128–7139.
[76] S. Ardizzone, G. Fregonara, S. Trasatti, Inner' and 'outer' active surface of RuO_2 electrodes, Electrochim. Acta 35 (1990) 263–267.
[77] L. Negre, B. Daffos, P.L. Taberna, P. Simon, Solvent-free electrolytes for electrical double layer capacitors, J. Electrochem. Soc. 162 (2015) A5037–A5040.
[78] J. Shao, X. Zhou, Q. Liu, R. Zou, W. Li, J. Yang, J. Hu, Mechanism analysis of the capacitance contributions and ultralong cycling-stability of the isomorphous MnO_2@MnO_2 core/shell nanostructures for supercapacitors, J. Mater. Chem. A 3 (2015) 6168–6176.
[79] C.P. De Pauli, S. Trasatti, Electrochemical surface characterization of IrO_2 + SnO_2 mixed oxide electrocatalysts, J. Electroanal. Chem. 396 (1995) 161–168.
[80] C. Du, N. Pan, Supercapacitors using carbon nanotubes films by electrophoretic deposition, J. Power Sources 160 (2006) 1487–1494.
[81] C.W. Huang, Y.T. Wu, C.C. Hu, Y.Y. Li, Textural and electrochemical characterization of porous carbon nanofibers as electrodes for supercapacitors, J. Power Sources 172 (2007) 460–467.
[82] A. Shanmugavani, R.Kalai Selvan, Synthesis of $ZnFe_2O_4$ nanoparticles and their asymmetric configuration with $Ni(OH)_2$ for a pseudocapacitor, RSC Adv. 4 (2014) 27022–27029.
[83] K.V. Sankar, R.K. Selvan, The preparation of $MnFe_2O_4$ decorated flexible graphene wrapped with PANI and its electrochemical performances for hybrid supercapacitors, RSC Adv. 4 (2014) 17555–17566.
[84] J. Zhang, H. Feng, Q. Qin, G. Zhang, Y. Cui, Z. Chai, W. Zheng, Interior design of three-dimensional CuO ordered architectures with enhanced performance for supercapacitors, J. Mater. Chem. A. 4 (2016) 6357–6367.
[85] A.K. Arof, S. Amirudin, S.Z. Yusof, I.M. Noor, A method based on impedance spectroscopy to determine transport properties of polymer electrolytes, Phys. Chem. Chem. Phys. 16 (2014) 1856–1867.
[86] S. Buathet, K. Simalaotao, P. Reunchan, V. Vailikhit, P. Teesetsopon, D. Raknual, N. Kitisripanya, A. Tubtimtae, Electrochemical performance of Bi_2Te_3 heterostructure thin film and Cu_7Te_4 nanocrystals on undoped and In^{3+}-doped WO_3 films for energy storage applications, Electrochim. Acta 341 (2020) 136049.
[87] Y. Honda, T. Haramoto, M. Takeshige, H. Shiozaki, T. Kitamura, M. Ishikawa, Aligned MWCNT sheet electrodes prepared by transfer methodology providing high-power capacitor performance, Electrochem. Solid State Lett. 10 (2007) A106–A110.
[88] P. Noppakuadrittidej, V. Vailikhit, P. Teesetsopon, S. Choopun, A. Tubtimtae, Copper incorporation in Mn^{2+}-doped Sn_2S_3 nanocrystals and the resultant structural, optical, and electrochemical characteristics, Ceram. Inter. 44 (2018) 13973–13985.
[89] Z. Yu, B. Duong, D. Abbitt, J. Thomas, Highly ordered MnO_2 nanopillars for enhanced supercapacitor performance, Adv. Mater. 25 (2013) 3302–3306.
[90] M.T. Andreuccetti, B.S. Leite, J.V.H. D'Angelo, Density, viscosity, solids and sodium sulfate contents revisited, O. Papel. 72 (2011) 52–57.
[91] F.G. Wilhelm, N.F.A. van der Vegt, M. Wessling, H. Strathmann, Chronopotentiometry for the advanced current–voltage characterisation of bipolar membranes, J. Electroanal. Chem. 502 (2001) 152–166.
[92] V. Knap, D.I. Stroe, M. Swierczynski, R. Teodorescu, E. Schaltz, Investigation of the Self-discharge Behavior of Lithium-Sulfur Batteries, J. Electrochem. Soc. 163 (2016) A911–A916.
[93] D. Bresser, S. Passerini, B. Scrosati, Recent progress and remaining challenges in sulfur-based lithium secondary batteries–a review, Chem. Commun. 49 (2013) 10545–10562.